Static and Dynamic Wetting Behavior of Drops on Impregnated Structured Walls by Molecular Dynamics Simulation

Stefan Becker,[†] Maximilian Kohns,[†] Herbert M. Urbassek,[‡] Martin Horsch,[*,†] and Hans Hasse[†]

[†]*Laboratory of Engineering Thermodynamics, University of Kaiserslautern, Kaiserslautern, Germany*

[‡]*Physics Department and Research Center OPTIMAS, University of Kaiserslautern, Kaiserslautern, Germany*

E-mail: martin.horsch@mv.uni-kl.de

Abstract

Nanoscale drops on structured walls with which they interact through dispersive forces are investigated by molecular dynamics simulation. The drops are in the impregnation wetting regime and the influence of the structures on the static and the dynamic wetting properties is studied. Drops of different size are simulated on six different walls which vary in the structure size and the wall morphology. Due to the nanoscale structure, there is a deviation of the interfacial tensions between the fluid and the wall from the value which would be observed on a macroscopic length scale. This phenomenon leads to contact angles which are greater than those predicted by the Cassie model. Accounting for the deviation of the interfacial tensions, the Cassie model is confirmed for drops on homogeneously structured walls but it is shown to be inadequate for inhomogeneously structured walls. The dynamics of drop spreading is analyzed. It is observed that the presence of the wall structure poses hurdles to the spreading dynamics. The speed of spreading slows down with increasing structure size. The mechanism of drop spreading is observed to happen via the formation of local liquid protrusions of the drop and subsequent broadening of the protrusions. In the stable state, drop configurations are found which break the symmetry imposed by the wall geometry.

1 Introduction

Wetting of solids plays an important role in many processes. The wetting behavior is often classified in terms of the contact angle $0° \leq \theta \leq 180°$ of a drop resting on a surface. For an ideal system, the Young equation[1] relates the intrinsic contact angle θ_0 with the interfacial free energies which arise from the molecular interactions of the involved materials. Much experimental work has been conducted to specify the contact angle of various solid–liquid combinations and there is a variety of models for the characterization of the interfacial free energies, often on the basis of molecular interactions.[2–11] Molecular simulations based on force fields are particularly suited for studying the wetting behavior of a liquid on a solid.[12–22]

Technical surfaces do not fulfill the prerequisites of the Young equation as they exhibit topographical or chemical heterogeneities which lead to complex wetting phenomena.[23,24] For example, when a drop rests on a geometrically structured surface, the hollows of the wall may be filled with gas or with liquid. The way the hollows are filled are designated by three distinct wetting states: In the "Cassie" state, the hollows underneath and beside the drop are filled with gas. In the "Wenzel" state, the hollows underneath the drop are filled with liquid and the ones beside the drop contain gas. The third wetting state is the "impregnation wetting state" which is characterized by the liquid filling the hollows underneath and beside the drop.[23] For clarity, it is noted here that both the Cassie and the impregnation wetting state may be described by the model of Cassie and Baxter[25] and the Wenzel model[26] may be applied to the Wenzel wetting state. Which one of the three wetting states is observed in an actual situation, depends on the topography of the solid surface and on the affinity between the solid and the fluid which is usually characterized by the intrinsic contact angle θ_0.

While there are many studies on the Cassie and the Wenzel wetting regimes,[20,23,25–34] the focus of the present work is on the less well studied impregnation wetting state. In that state, the filling of the surface structure may generally be accomplished by two mechanisms. If the surface structure is composed of an array of pillars, wicking of the fluid into the structure is observed.[35,36] If, however, the structure is formed by parallel grooves, wicking can not occur and the filling is expected to take place via capillary condensation of the vapor into the grooves.

The measurement of contact angles on technical surfaces reveals a difference between the advancing angle and the receding angle,[27,28,30,37–39] which is referred to as contact angle hysteresis: An inflation of the drop does not lead to immediate spreading. Instead, the contact line is pinned and does not move forward, so that the contact angle increases as the volume increases. Similarly, a deflation of the drop causes a decreasing contact angle. The hysteresis is a measure for the dependence of the contact angle on the history of the drop. Contact angle measurements on surfaces with tailor–made topographies reveal a relation between the hysteresis and the direction in which the contact line is forced to advance.[29,34] For example, the contact angle hysteresis on a surface which is structured by grooves arranged in form of concentric rings is rather large. On this surface, the spreading of the drop leads to a motion of the contact line perpendicular to the grooves. However, if a drop is inflated or deflated on a surface which is structured by straight star–like grooves forming channels which meet in the center, the contact line can move along the grooves and no hysteresis is observed,[29] i.e. there is no pinning of the contact line. The presence of the hysteresis also influences the spreading process of the drop. Experiments with drops on concentric grooves show a stick–slip motion of the contact line upon continuous inflation of the drop volume, while the stick–slip motion is not observed on a surface exhibiting star–like grooves.[29] The time scale on which the slip motion occurs is very short, which makes it hard to experimentally observe the microscopic mechanisms occurring during that motion.[34]

The description of the wetting properties of technical surfaces requires the understanding of the physical relationship between the microscopic structure of a surface and the contact angle. Wenzel[26] as well as Cassie and Baxter[25] developed the the first models that addressed the effect of topographical and chemical heterogeneity on the contact angle. The derivation of both models is essentially the same: They rely on the variation of the free energy of a system related to the change of the interfacial areas. There, the surface properties are represented by global averages over the entire surface. The Wenzel model and the model of Cassie and Baxter, which is referred to as the Cassie model in the following, for brevity, give qualitative information on the influence of the surface heterogeneity on the contact angle. That is, the models correctly predict an increase

or decrease of the contact angle caused by the surface heterogeneity. Under certain conditions,[40,41] quantitative agreement with experimentally determined contact angles is observed.[31]

Extrand[42] and Gao and McCarthy[43] carried out contact angle measurements on surfaces with inhomogeneously distributed surface structures. They show that both the Wenzel and the Cassie model fail to correctly predict the contact angle if the surface structure is inhomogeneously distributed. Based on the experimental results, they challenge the adequacy of the concept of interfacial free energies to describe the contact angle. Instead, they argue that there is an energetic state of the contact line which determines the contact angle.

Moreover, the models of Wenzel and Cassie are not suitable to explain the existence of contact angle hysteresis. As shown by Johnson and Dettre,[40,44] the contact angle hysteresis emerges from the chemical and topographical heterogeneities of the surface. To describe the hysteresis, the spatial distribution of the heterogeneity has to be accounted for. That way, the experimentally observed dependence of the contact angle hysteresis on the direction in which the contact line moves, i.e. along or perpendicular to a groove, can also be explained. In their studies, Johnson and Dettre considered drops resting on topographically or chemically structured model surfaces. They computed the free energy landscape of a system associated with various drop configurations and found metastable configurations which are separated by barriers in the free energy landscape. That is, the contact angle hysteresis on heterogeneous surfaces is related to free energy barriers. The contact angles corresponding to the global minimum of the free energy were those predicted by the Cassie or the Wenzel model, respectively. Johnson and Dettre also evaluated the height of the energy barriers based on the assumption that the drop maintains its spherical shape during the spreading process, i.e. the transition from one metastable configuration of the drop to the next configuration is accomplished by a "jump" of the entire contact line from one position to the next. This jumping of the contact line has also been observed in molecular dynamics (MD) and density functional theory (DFT) simulation studies.[45,46] This transition pathway, however, leads to very high energy barriers. De Gennes[47] instead proposed the local nucleation of a liquid protrusion and the subsequent broadening of the protrusion as the more realistic transition path, because the barrier is lower in

this case.

Using molecular simulations for studying wetting phenomena, predictive results of great detail are obtained which solely rely on the chosen scenario and the molecular force fields. There are two typical approaches to determine the contact angle using molecular simulations: From Monte Carlo (MC) simulation techniques, the average interfacial free energies are calculated, e.g. via transition matrix Monte Carlo simulations[48] or Gibbs–Cahn integration,[49] and the contact angle is obtained from one of the Cassie or Wenzel model,[20,50] whichever applies to the observed wetting state. In MD simulations usually, a drop on a wall is considered and the contact angle is obtained from the density profile of the fluid.

Molecular simulations offer the opportunity to study physical effects on the nanometer length scale where the values of the properties of matter may deviate from the corresponding macroscopic values due to finite size effects.[51–56] For example, it has been shown that confinement of a fluid in narrow cavities leads to a deviation of the the value of the interfacial tension from the value obtained in experiments using drops of macroscopic dimensions,[52,57–61] which are called macroscopic interfacial tensions, in the following. Nevertheless, the typical length scale of molecular simulations is sufficient to capture macroscopic wetting behavior.[17,21,62,63]

In a recent study of the authors, the nano–drop technique was used to systematically investigate the contact angles of sessile drops in Lennard–Jones systems by variation of the temperature, the solid–fluid interaction strength, and the density of the solid wall.[21] The impact of nanoscale roughness on the interfacial tensions and the contact angle in a system of the Lennard–Jones type has been studied in the group of Errington, using MC simulations based on an interface potential approach.[64,65] For walls with parallel grooves, they observed a decrease of the absolute value of the solid–liquid and solid–vapor interfacial tensions with decreasing groove dimensions. That is, the value of the tensions is found to deviate from that of a macroscopic setting where the the interfacial tension does not depend on the groove dimension. In that study, most of the contact angles observed on lyophilic walls ($\theta_0 < 90°$) are found to be smaller than the intrinsic contact angle. This is in qualitative agreement with the models of Wenzel and Cassie, which always predict a decrease

of the contact angles on rough lyophilic walls. However, the decrease of the contact angles was not as high as predicted by the models, in line with findings from a MD simulation study by Yong and Zhang.[33] This quantitative deviation is attributed to the variation of the interfacial tensions with the size of the nano–grooves, as mentioned above. For very narrow rectangular grooves of a width less than about 2 σ (where σ is the Lennard–Jones size parameter, cf. Section 3), Kumar and Errington[65] observed contact angles even larger than the intrinsic angle, which is opposite to the predictions of the models of Wenzel and Cassie. This observation is confirmed by results of other molecular simulation and density functional theory (DFT) studies.[66–69] Leroy and Müller–Plathe[70] observed a similar behavior for water on structured surfaces.

MD simulations are particularly well suited to capture both the contact angle in the steady state and the dynamics during the spreading process. For example, Svoboda et al.[69] observed a diffusive motion of a drop on a structured surface during the sprading and in the stationary state. Li et al.[71] recently used MD simulation to study the combined effect of fluid–wall affinity, surfactants and the wall structure on the wetting behavior in a model system. For a single wall structure consisting of an array of pillars, the Cassie and the Wenzel wetting state are observed upon changing the solid–fluid interaction strength. The presence of the surfactant leads to a decrease of the static contact angle on a plane wall, irrespective of the solid–fluid interaction strength. In the presence of a wall structure, the surfactant only influences the static contact angle of the lyophobic ($\theta_0 > 90°$) walls, while the static contact angle on the lyophilic wall is not changed by the presence of the contact angle. In that study, the spreading process is also monitored. On the structured wall, wicking of the fluid is observed accompanied by a stick–slip like motion of the contact line.

Most of the molecular simulation studies that investigate the contact angle on structured surfaces use a two dimensional wall topography, i.e. the wall is structured by parallel grooves. In some DFT or MD simulations, the periodic boundary conditions are employed to replace the liquid drop by a liquid cylinder of infinite length.[45,46,72]

In the present work, the static and the dynamic wetting properties of sessile drops on geometrically structured surfaces are studied by MD simulations. The walls are chemically homogeneous

and the structure is formed by concentric grooves of rectangular cross section and radial symmetry. Different wall morphologies are considered. The drops start spreading from an initial configuration until a stable state is obtained where the system is in the impregnation wetting regime. The mechanisms are elucidated by which the impregnation wetting state establishes and by which the contact line advances over the surface structures. In the light of the hysteretic effects observed in wetting, several drops of varying size are considered for each of the walls in order to obtain significant results. The results on the static contact angle are compared to the prediction of the Cassie model. It is examined to what extend the Cassie model can be applied to nano–structured surfaces.

The paper is organized as follows: In Section 2, the Cassie model is introduced. In Section 3, the molecular model, the simulation scenarios, and the simulation method are described. The simulation results are discussed in Section 4. Conclusions are drawn in Section 5.

2 Theory

The Young equation[1] relates the intrinsic contact angle θ_0 on an ideally plane and homogeneous solid surface to the interfacial tensions of the liquid–vapor, solid–vapor, and solid–liquid interfaces, γ_{lv}, γ_{sv}, and γ_{sl}, respectively,

$$\cos\theta_0 = \frac{\gamma_{\mathrm{sv}} - \gamma_{\mathrm{sl}}}{\gamma_{\mathrm{lv}}}. \tag{1}$$

Eq. (1) can be obtained from a minimization of the interfacial free energy F^γ of the three interfaces

$$\mathrm{d}F^\gamma = \gamma_{\mathrm{sl}}\mathrm{d}A_{\mathrm{sl}} + \gamma_{\mathrm{sv}}\mathrm{d}A_{\mathrm{sv}} + \gamma_{\mathrm{lv}}\mathrm{d}A_{\mathrm{lv}}, \tag{2}$$

where the A_{ij} are the areas of the three interfaces. A displacement of the contact line results in a change of the interfacial areas which is related by $\mathrm{d}A_{\mathrm{sv}} = -\mathrm{d}A_{\mathrm{sl}}$ and $\mathrm{d}A_{\mathrm{lv}} = \cos\theta_0\ \mathrm{d}A_{\mathrm{sl}}$.

The Cassie model[25] is used to describe the contact angle on plane and chemically heterogeneous surfaces. For a surface that is built of two chemically different kinds of surface patches i and j, the Cassie model reads

$$\cos\theta_{\mathrm{C}} = \phi\cos\theta_i + (1-\phi)\cos\theta_j, \tag{3}$$

where θ_i is the intrinsic contact angle on the surface of kind i and θ_j is the intrinsic contact angle on the surface of kind j. ϕ is the fraction of the surface area formed by the patches of type i relative to the total surface area. Note that ϕ does not account for the spatial distribution of the two different patches. It is a property which represents an average over the entire surface. Eq. (3) is a general form of the Cassie model for a surface composed of two types of surface patches. The parameters in this equation have to be adjusted to the particular situation at hand.

The main focus of the present work is on the impregnation wetting state. In this case, the surface can be considered plane and composed of solid and liquid patches. Following Bico et al.,[32] the contact angle is described by the Cassie model, with the average fraction ϕ of the solid surface area and the intrinsic contact angle θ_0 which a liquid drop assumes on the solid. Since the liquid

does not form a contact angle with itself ($\cos\theta = 1$), Eq. (3) transforms to

$$\cos\theta_{\mathrm{C}} = 1 + \phi(\cos\theta_0 - 1). \tag{4}$$

Eq. (4) is the form of the Cassie model that is applied to the impregnation wetting state.[32] In the following, the derivation of the Cassie model in form of Eq. (4) is considered in detail, to discuss its validity for nanoscopic phenomena. Like the Young equation, the Cassie model is derived from an energy balance. The variation of the the interfacial areas, i.e. a displacement of the contact line, changes the interfacial free energy

$$\mathrm{d}F^{\gamma} = \gamma_{\mathrm{sl}}\phi\mathrm{d}A_{\mathrm{sl}} - \gamma_{\mathrm{sv}}\phi\mathrm{d}A_{\mathrm{sl}} - \gamma_{\mathrm{lv}}^{(\mathrm{g})}(1-\phi)\mathrm{d}A_{\mathrm{sl}} + \gamma_{\mathrm{lv}}^{(\mathrm{d})}\cos\theta\mathrm{d}A_{\mathrm{sl}}, \tag{5}$$

where $\gamma_{\mathrm{lv}}^{(\mathrm{g})}$ denotes the interfacial tension of the liquid–vapor interfaces covering the grooves and $\gamma_{\mathrm{lv}}^{(\mathrm{d})}$ the interfacial tension of the spherical surface of the drop. For minima of the interfacial free energy ($\mathrm{d}F^{\gamma}/\mathrm{d}A_{\mathrm{sl}} = 0$) , Eq. (5) yields:

$$\gamma_{\mathrm{lv}}^{(\mathrm{d})}\cos\theta = (\gamma_{\mathrm{sv}} - \gamma_{\mathrm{sl}})\phi + (1-\phi)\gamma_{\mathrm{lv}}^{(\mathrm{g})}. \tag{6}$$

The sum on the right hand side of Eq. (6) represents contributions to the free energy which arise from the planar surface. In the following, this term is defined as the average surface–fluid (Sf) free energy per unit area

$$\mathcal{F} = (\gamma_{\mathrm{sv}} - \gamma_{\mathrm{sl}})\phi + (1-\phi)\gamma_{\mathrm{lv}}^{(\mathrm{g})}. \tag{7}$$

The contact angle is related to $\mathcal{F}$ via Eq. (6)

$$\cos\theta = \frac{\mathcal{F}}{\gamma_{\mathrm{lv}}^{(\mathrm{d})}}. \tag{8}$$

If the interfacial tensions $\gamma_{\mathrm{lv}}^{(\mathrm{g})}$ and $\gamma_{\mathrm{lv}}^{(\mathrm{d})}$ are equal, Eqs. (6) and (8) simplify, as $(\gamma_{\mathrm{sv}} - \gamma_{\mathrm{sl}})/\gamma_{\mathrm{lv}}^{(\mathrm{d})}$ can be replaced by $\cos\theta_0$ and $\gamma_{\mathrm{lv}}^{(\mathrm{g})}/\gamma_{\mathrm{lv}}^{(\mathrm{d})}$ is unity. This leads directly to the Cassie model in form of

Eq. (4).

Which state, the Wenzel state or the impregnation wetting state, is observed on a geometrically structured lyophilic ($\theta_0 < 90°$) surface, depends on thermodynamic conditions. The thermodynamic condition for the establishment of the impregnation wetting state is given by[32]

$$\cos\theta_0 > \frac{1-\phi}{r-\phi}, \tag{9}$$

where r is the roughness parameter of the Wenzel model, i.e. the ratio between the total area of the geometrically structured surface and its projected area. ϕ is the fraction of the plane surface that is formed by the solid and $(1-\phi)$ is the fraction formed by the liquid. Like the parameter ϕ, r is a surface parameter which represents an average over the entire surface.

Note that Eqs. (1) to (8) are solely based on energetic considerations and, hence, they are independent from the particular choice of the molecular model.

3 Molecular Model, Simulation Method, and Simulation Scenarios

3.1 Molecular Model

The truncated and shifted Lennard–Jones (LJTS) potential[73] with a cutoff radius $r_c = 2.5\ \sigma$,

$$u(r_{ij})^{\mathrm{LJTS}} = \begin{cases} u^{\mathrm{LJ}}(r_{ij}) - u^{\mathrm{LJ}}(r_c), & r_{ij} < r_c \\ 0, & r_{ij} \geq r_c \end{cases}, \tag{10}$$

where

$$u^{\mathrm{LJ}}(r_{ij}) = 4\,\epsilon \left(\left(\frac{\sigma}{r_{ij}} \right)^{12} - \left(\frac{\sigma}{r_{ij}} \right)^{6} \right) \tag{11}$$

is used to describe the dispersive and the repulsive interaction between pairs of fluid particles as well as between a fluid particle and a wall particle. The position of the solid particles is fixed in the present work. The application of the LJTS potential in molecular simulations enables the efficient simulation of a large number of particles, while the bulk and the interfacial properties of simple fluids are well described, if appropriate values for the size and energy parameters σ and ϵ, respectively, are chosen.[74]

As shown in a previous study of the authors,[21] the intrinsic contact angle θ_0 strongly depends on the density of the wall ρ_s, the LJ energy parameter of the solid–fluid (sf) interaction ϵ_{sf}, and the temperature T of the system. In the present study, these parameters are chosen as to obtain an intrinsic contact angle of 55°, cf. Section 4.1. According to Eq.(9), this leads to the impregnation wetting state for the walls considered in the present study.

The solid is represented by a face-centered cubic lattice, the (100) surface exposed to the fluid, with a density of $\rho_s = 1.07\ \sigma^{-3}$, where σ refers to the LJ size parameter of the fluid–fluid interaction. The energy parameter of the unlike interaction is scaled by $\epsilon_{sf} = 0.65\ \epsilon$, where ϵ refers to the LJ energy parameter of the fluid–fluid interaction. The temperature is chosen to be $T = 0.8\ \epsilon/k$ which is about half way between the triple point temperature[75] $0.65\ \epsilon/k$ and the critical temperature[74]

1.08 ϵ/k of the LJTS fluid, where k is the Boltzmann constant. The size parameter of the solid–fluid interaction was chosen equal to that of the fluid $\sigma_{sf} = \sigma$, in the present work, which has a minor influence on the contact angle.[21] The chosen potential parameters and the temperature are the same for all simulations of the present work, as solely the influence of the wall morphology on the contact angle is studied.

3.2 Simulation Scenarios

In the present study, 28 scenarios were studied by MD simulations. In all scenarios but one, a drop with an initial contact angle of 90Âř is spreading until a stationary state is reached. The evolution of the contact angle is monitored over time. That way, information on both the static and the dynamic contact angle is obtained from a single simulation run. The scenarios differ in the type of the structure of the wall and the size of the drop.

In one additional scenario the initial conditions are changed such that a liquid slab completely covers the wall at the start of the simulation. This scenario serves as a check to what extend the initial conditions influence the contact angle in the stationary state.

The principle set up of the simulation scenarios is sketched in Figure 1. The wall is located in the x, z–plane of a cartesian coordinate system in which the y–axis is perpendicular to the wall. The grooves in the wall are arranged as concentric rings. Two cylindrical coordinates are used here: In the wall–fixed coordinate system, the y–axis coincides with the symmetry axis of the grooves. The wall–fixed coordinate system is solely used for determining the fluid structure in vicinity of the wall. In the drop–fixed coordinate system, the y–axis follows the lateral motion of the drop over time. It is used for characterizing the drop by its radius $\mathcal{R}$ and the contact angle θ. From these two quantities, the contact line radius is calculated via

$$R_{sl} = \mathcal{R} \sin\theta \tag{12}$$

and the drop volume via

$$V = \frac{\pi}{6}\mathcal{R}^3(1-\cos\theta)\left(3\sin^2\theta + (1-\cos\theta)^2\right). \tag{13}$$

Note, that only the liquid above the wall is considered part of the drop volume, but not the liquid in the grooves.

In all but a single scenario, which is introduced later in the section, the initial configuration is as follows: The liquid phase is placed in form of a sphere cap of radius $\mathcal{R}^{(0)}$ and a contact angle of 90° on the wall. The axis of rotational symmetry of the sphere cap coincides with the symmetry axis of the concentrically arranged grooves. The sphere cap is surrounded by a vapor phase. The particles of both fluid phases are arranged on regular lattice sites and the density of both phases is chosen according to their values at saturation.[74] The grooves in the wall are initially free of fluid particles.

With the start of the simulation, the drop starts to spread or contract. The temporal evolution of the contact angle and the drop configurations are monitored during the simulation. After equilibration, the simulation scenarios also yield the results on the stationary wetting state. In the present study, the equilibration time is taken as the time during which the contact angle and the drop volume vary and the equilibration process is finished when both quantities reach a stationary value. After the equilibration, the simulation results in the stationary state are determined during another 6 million time steps. As the particular simulation scenarios differ, the total simulation time differs between 9 million and up to 31 million time steps.

The six walls that are studied in the present work are structured by rectangular grooves which are arranged as concentric rings. The groove width is B, its depth is H. There are three different wall types which vary in their structure, cf. Figure 2. The type I walls have grooves on the entire surface, the type II walls have groove only in the central region and are flat outside, the type III walls are flat in the center and have grooves outside. The radius of the central region is R_{center}, where R_{center} is defined as shown in Figure 2. There are two walls of each type which vary in the

groove width. The groove width is either $B = 2\,\sigma$ or $B = 6\,\sigma$, while the depth H of the grooves is 4.7 σ throughout. The rims separating the grooves have the same width B as the grooves, i.e. the periodicity of a structural pattern is $2B$. Table 1 gives a survey of the different walls.

The particular walls are labeled here by their type and the width of the grooves. For example, the homogeneously structured wall of type I with grooves of width $B = 6\sigma$ is labeled I–6, while the wall of type II with grooves of width $B = 2\sigma$ is labeled II–2. A particular simulation scenario is specified by the drop radius in the initial state, i.e. by $\mathcal{R}^{(0)}$, and by the particular wall. For example, the scenario I–6.25 refers the drop with an initial radius of 25 σ on the wall I–6.

A single scenario is considered in which the initial configuration is different from the other scenarios. There, the fluid particles are arranged in form of a liquid slab which initially covers the entire wall I–6. The scenario is named I–6.∞. It yields the receding contact angle of the drop and, thus, it serves as a check of the contact angle dependence on the initial configuration. Wall I-6 is chosen, as one would expect it to exhibit the largest hysteresis of all the walls considered in the present work. Like in the other scenarios, the fluid particles are initially placed on regular lattice sites, and the grooves of the wall are free of fluid particles. Above the liquid slab, there are initially no particles. The vapor phase is generated by evaporation of the liquid slab at the begin of the simulation.

The roughness parameter r of the walls is defined as the ratio between the total surface area and the projected surface area. The roughness parameter of wall I–6 is $r = 1.8$ and for wall I–2 it is $r = 3.4$. As the rims and the grooves have the same width B, the solid surface fraction is $\phi = 0.5$ for both walls I–6 and I–2. Details on the calculation of r and ϕ are given in the Supporting Information.

The suitability of the Cassie model to predict contact angles on inhomogeneously structured walls, such as the walls of type II and type III, is tested by comparison of the simulation results in the stationary state to the prediction of the Cassie model. The inhomogeneously structured walls may by regarded as composed of two different surface patches. One patch is the plane surface on which a liquid drop assumes the intrinsic contact angle θ_0. The other patch is the geometrically

structured surface where a characteristic contact angle θ_{str} is found. This contact angle θ_{str} is not a prediction of the Cassie model, but it is the angle which is observed in the MD simulations for the drops on the homogeneously structured surfaces of type I. The fraction of the wetted area (i.e. the area beneath the drop) of the structured surface patch relative to the total wetted area is denoted here by ϕ_{str}. The so characterized inhomogeneous surfaces may be described by the Cassie model. In this situation, Eq. (3) yields

$$\cos\theta_{\mathrm{str}} = \phi_{\mathrm{str}} \cos\theta_{\mathrm{str}} + (1 - \phi_{\mathrm{str}}) \cos\theta_0. \tag{14}$$

From the simulation results in the stationary state, the contact line radius R_{sl} of the drops is obtained from which the value of the parameter ϕ_{str} is determined. As the drops on the type II walls cover the structured part in the middle, the fraction of the central area relative to the total wetted area is

$$\phi_{\mathrm{str}}^{(\mathrm{II})} = \frac{R_{\mathrm{center}}^2}{R_{\mathrm{sl}}^2}. \tag{15}$$

The drops on the walls of type III cover the plane surface in the middle. There, the fraction of the wetted structured area relative to the total wetted area is

$$\phi_{\mathrm{str}}^{(\mathrm{III})} = 1 - \frac{R_{\mathrm{center}}^2}{R_{\mathrm{sl}}^2}. \tag{16}$$

3.3 Simulation Method

MD simulations are carried out in the canonical (N, V, T) ensemble with the massively parallel software *ls1 mardyn*.[76] Newton's equations of motion are solved using the Verlet leapfrog algorithm with a time step length of 0.001 $\sigma\sqrt{m/\epsilon}$, where m is the mass of a fluid particle. To improve legibility of the text in the following, the numerical values of the time are given as a multiple of $\tilde{t}$, where

$$\tilde{t} = 1000\, \sigma\sqrt{m/\epsilon}. \tag{17}$$

Hence, a time of $t = 1\ \tilde{t}$ corresponds to one million time steps for the time step length chosen in the present study. The temperature is controlled using the Andersen thermostat[77] with a collision frequency of $\nu = 0.05$. The parallelisation is accomplished with a spatial decomposition based on a k–dimensional tree. Periodic boundary conditions are applied in all directions leaving a channel for the fluid between the wall and its periodic image, cf. Figure 1. The height of the channel exceeds 40 σ in all cases, which avoids finite size effects related to the channel height.[78]

In all cases, the thickness of the wall is two and a half crystal unit cells or more. This exceeds the cutoff radius of the fluid and avoids periodic artifacts, which could be caused by an interaction of fluid particles on different sides of the wall. The total number of particles varies between $7.4 \cdot 10^4$ and $2.9 \cdot 10^5$ and the number of fluid particles varies between $2.6 \cdot 10^4$ and $1.3 \cdot 10^5$. The size of the simulation box is adapted to the different scenarios. Information on the number of particles and the box dimensions for each scenario are given in the Supporting Information.

Local density profiles of the fluid are determined over the cylindrical coordinates R and y in both the drop–fixed and the wall–fixed coordinate systems. The local density profiles $\rho_\mathrm{f}(R, y)$ are constructed for discrete bins employing a bin size of 0.1 σ in y–direction and a varying bin size in R–direction.[21] The drop–fixed density profile is used to obtain the contact angle θ of the drop. This is accomplished by fitting a sphere of radius $\mathcal{R}$ to the the vapor–liquid interface at the locations where the density equals the arithmetic mean $(\rho' + \rho'')/2$ between the bulk value of the liquid density ρ' and the bulk value of the vapor density ρ'' which are known from previous studies.[74] The tangent to the circle at the intersection with the top layer of the wall gives the contact angle. The instantaneous contact angle is obtained from a single density profile which is an average over $5 \cdot 10^5$ time steps. The numerical values of the contact angles in the stationary state represent the average contact angle over 6 million time steps. The uncertainty of the contact angle in the stationary state is estimated by the standard deviation of the instantaneous θ values.

4 Results and Discussion

4.1 Intrinsic Contact Angle

In a separate simulation of a drop on a plane wall, the intrinsic contact angle is determined for the set of simulation parameters chosen throughout the present work. The number of fluid particles in this simulation is 58200. In the stationary state, the drop has a contact angle $\theta_0 = (55 \pm 1)°$, a volume $V = (58.2 \pm 0.2) \cdot 10^3\ \sigma^3$ and a contact line radius $R_{sl} = (40.4 \pm 0.5)\ \sigma$.

4.2 Stationary Wetting of Structured Walls

4.2.1 Drop Shapes and Fluid Density Profiles

The simulation snapshots presented in Figure 3 show the typical shape of drops in the stationary state. For visualization purposes, the materials are represented by an isosurface based on a volumetric Gaussian density map.[79] In all cases, the drop surface exhibits roughness on a short length scale of a few σ which represents the typical fluctuations of fluid interfaces.[80] An even liquid–vapor interface is recovered by averaging over time. The drop in scenario I–2.32 (Figure 3, a) has the shape of a rough sphere cap while its position is off center with respect to the symmetry axis of the wall. The spherical drop shape is retained for all drops on the walls with a groove width of 2 σ (walls I–2, II–2, and III–2) as well as on the wall II–6, where the contact line resides on the plane part. The behavior of the drops on the walls I-6 and III-6 is different: For example, the drop in scenario I–6.38 (Figure 3, c) does not have a shape of a sphere cap. The drop is asymmetric and forms a protrusion which partly covers the groove adjacent to the drop. Consequently, the drop does not obey the symmetry imposed by the wall structure and the position of the drop, i.e. its center of mass, is not aligned with the axis of rotational symmetry of the wall. These asymmetries are observed for most of the drops on the walls I–6 and III–6 (cf. Figure 3, c-e). Only in a few scenarios,e.g. scenario I–6.32 (Figure 3, b), the drops are found to cover a groove completely without forming liquid protrusions. In those few cases, the drops are symmetric and obey the wall symmetry. Figure 3

(b-e) shows snapshots of drops on wall I–6 in the order of increasing liquid volume. It is observed, that the symmetry of the drops depends on their size. The smallest of the four drops (scenario I–6.32), shown in Figure 3(b), is symmetric. With increasing liquid volume, the drop shape becomes asymmetric. Liquid protrusions bridge part of the groove. The circumferential extent of the protrusions increases with increasing drop volume (Figure 3, b and c), until a symmetric drop shape is reached again, as can be anticipated form the snapshot of scenario I–6.40 (Figure 3, d). Drops which obey the cylindrical symmetry of the wall do so, because their surface-fluid interfacial area fits the discrete structure of the wall. That is, the drop symmetry is subject to periodic size effects.

As the density profiles of the fluid are determined in terms of the radial coordinate R and the axial coordinate y, they do not locally resolve the liquid protrusions. Instead, the protrusions are part of the density average along the circumferential direction. Figure 4 shows the density profile of the fluid in the scenario I–6.38 in the wall–fixed (top) and in the drop–fixed (bottom) coordinate system in the stationary state. In the wall–fixed coordinate system, the liquid–vapor interface of the drop in vicinity to the wall appears broader than at the apex of the drop. The broadening is caused by the asymmetric shape of the drop. It is less pronounced in the density profile in the drop–fixed coodinate system, Figure 4 (bottom), which is used for the determination of the contact angle. There, the profile of the fluid in the grooves is blurred, because the drop–fixed coordinate system is not aligned with the symmetry axis of grooves.

In the density profile in the wall–fixed coordinate system (Figure 4, top), the layer–like structure of the liquid in vicinity of the wall is readily discernible. This ordering decays with increasing distance from the wall. Aside the drop, the solid–vapor interface can be seen: There is an adsorbed fluid layer on top of the rims. The grooves are filled with fluid and covered by a liquid–vapor interface, i.e. the system is in the impregnation wetting state. Figure 5 (top) shows the density profile in the wall–fixed coordinate system close to the structural patterns of the wall I–6. The liquid in the grooves exhibits an ordered structure which is most pronounced in immediate vicinity to the wall and which decays towards the middle of the groove. It can be assumed that this ordering influences all thermodynamic properties of the liquid inside the grooves, especially the interfacial tension,

just as it does for the density. The grooves of the wall I–2 are also filled with fluid particles, cf. Figure 5 (bottom). As the grooves are very narrow, the ordering of the fluid does not decay, which indicates even stronger deviations from the bulk liquid properties and, hence, from the interfacial properties that would be observed on a macroscopic length scale. The fluid structure within the grooves, presented here for the walls of type I–6 and I–2, is also found for the liquid in the grooves of the walls of type II and type III. It is governed by the width of the grooves.

4.2.2 Contact Angles on Type I Walls

Several drops of different size are simulated on the walls I–6 and I–2 and the static contact angles θ observed in the different scenarios along with the drop volumes V and the radii of the contact line R_{sl} are given in Table 2.

The static contact angles found for the drops on the wall I-âĂŞ6 vary in the range between 42° and 45° which is smaller than the intrinsic contact angle ($\theta_0 = 55°$). The average value of the contact angles on wall I–6 is $\theta = 44°$. The contact angles of the drops on wall I–6 vary in a narrow range, which even holds for the scenario I–6.∞. This is noteworthy, since the different initial conditions in scenario I–6.∞ lead to a purely receding motion of the contact line during equilibration and one would expect a contact angle which is different from that of the other scenarios. Thus, the narrow range of observed contact angles indicates small contact angle hysteresis and, hence, small barriers in the free energy, for the scenarios considered in the present work.

The average value of the contact angle on wall I–6 ($\theta = 44°$) agrees well with the results of Kumar et al.,[65] who found a contact angle of 43° on a wall similar to the wall I-6. In the study of Kumar et al., the contact angle is predicted from the global minimum of the interfacial free energies which are determined with a MC simulation sampling scheme. The good agreement between the result of Kumar et al. and the results of the present study which rely on the evaluation of the density profile of actual drops shows that the description of the contact angles based on average interfacial free energies is valid for scenarios like that on the wall IâĂŞ6, where the surface structure is homogeneously distributed.

Qualitatively, the observed decrease of the contact angle with respect to the intrinsic contact angle is expected from the Cassie model in Eq. (4). The Cassie model, however, predicts a contact angle of $\theta_C = 38°$ for the scenarios on wall I–6 which is smaller than the value found in the present study. The deviation can be interpreted using the density profile of the fluid, cf. Figure 5 (top). Due to the topography of the wall, the liquid is confined in the grooves and it exhibits an ordered structure which is known to cause deviations from the liquid bulk properties.[51–55] As a consequence, the interfacial tension of the liquid–vapor interface covering the grooves decreases.[57–61] Similarly, the solid–liquid and the solid–vapor interfaces at the plateaus of the rims are interrupted by the interjacent liquid phase, which might cause deviations of the respective interfacial tensions.

In case of lyophilic surfaces it has been shown in previous molecular simulation studies that the value of γ_{sv} is much smaller than the value of γ_{sl}.[64,66,81] Moreover, for a liquid wetting a nano–grooved surface, Leroy and Müller–Plathe[82] showed that the absolute value of the solid–liquid interfacial tension may vary in a non–monotonous way as the number of grooves per unit area is increased. Above a certain number of grooves per unit area, the absolute value of the solid–liquid interfacial tension decreases. As a consequence, the confinement of the liquid in the grooves leads to a diminution of the average surface–fluid free energy per unit area $\mathcal{F}$, cf. Eq. (7), as compared to the value of $\mathcal{F}$ that is obtained when macroscopic interfacial free energies are introduced. The diminution of $\mathcal{F}$ yields a decrease of $\cos\theta$ or, equivalently, an increase of θ as compared to the "macroscopic situation". This explains the larger contact angles compared to the prediction of the Cassie model which are observed in the present simulations. The prediction of Eq. (4) and the simulation results differ 9 % in terms of the average surface–fluid free energy per unit area $\mathcal{F}$.

The contact angles found for different drops on the wall I–2, vary between 55° and 59° and the average value is 57°, cf. Table 2. Here, the surface structure leads to contact angles which are slightly greater than the intrinsic contact angle, which has also been found in other molecular simulation and DFT studies.[65–69] This effect of the surface structure cannot be captured by the Cassie model, as it always predicts a smaller contact angle for the impregnation state, namely $\theta_C = 38°$ for the scenarios on wall I–2. The present results are attributed to a shift of the interfacial

tensions and, hence, of $\mathcal{F}$ caused by the confinement of the fluid in the narrow grooves, cf. Figure 5 (bottom). Comparison to the scenarios on wall I–6 shows that the stronger confinement of the fluid in the scenarios on wall I–2 leads to a smaller value of $\mathcal{F}$. Comparison of Eq. (8) with the Young model, i.e. Eq. (1), reveals that $\mathcal{F}$ is 5 % smaller than the difference $(\gamma_{sv} - \gamma_{sl})$ which determines the contact angle on a plane wall.

4.2.3 Contact Angles on Type II Walls

In the simulations of drops on the walls of type II, the contact line is initially located on the planar part of the wall and the drops initially cover the grooves. In the stationary state, the grooves are filled with fluid. During the simulation, the drops exhibit diffusive motion. However, they remain at about their initial position, i.e. they do not diffuse away from the wall structure and do not uncover the grooves. The contact angles found on wall II–6 are between 53 and 55°, the average value is 54°, cf. Table 2. The contact angles found on wall II–2 are between 55° and 56°, the average value is 55°. Hence, for both walls, no significant deviation from the intrinsic contact angle $\theta_0 = 55°$ is observed. The variation of the width or the number of the grooves (two grooves in the case of wall II–6 and six grooves in case of wall II–2) shows no significant impact on the contact angle.

4.2.4 Contact Angles on Type III Walls

On the walls of type III, the contact line is located on the structured part of the surface and the center of the solid–liquid interface is located on the plane part of the wall. The simulation results for the inhomogeneously structured walls III–6 and III–2 are summarized in Table 2. For the wall III–6, the contact angles vary between 41° and 46°, which is essentially the same range of contact angles as observed for the corresponding homogeneously structured wall I–6. The drops on wall III–2 have contact angles of 56° and 58°. Again, these values correspond to the contact angles on the homogeneously structured wall I–2.

4.2.5 Comparison of Contact Angles on Tpye I, Type II and Type III Walls

The applicability of the Cassie model to wetting of inhomogeneously structured walls is tested by comparison of the simulation results with the prediction of Eq. (14). The intrinsic contact angle θ_0 is introduced into Eq. (14) to represent the plane part of the walls. The structured part of the walls is represented by the average contact angles observed on the homogeneously structured walls. That way, the variation of the interfacial tensions due to the confinement is accounted for. Hence, for the walls II–2 and III–2, the average contact angle of 57° found on wall I–2 is introduced for θ_{str} in Eq. (14). For the walls II–6 and III–6, the average contact angle of 44° found on wall I–6 is introduced for θ_{str} in Eq. (14).

Figure 6 shows the comparison of the simulation results and the prediction of Eq. (14). As expected, the Cassie model does not recover the simulation results. It predicts a variation of the contact angle with the variation of ϕ_{str}, i.e. with R_{sl}, while the simulation results do not show this behavior. That is, the surface morphology in vicinity of the contact line is crucial for the establishment of the contact angle, which confirms the experimental results of Extrand[42] and Gao and McCarthy.[43] The observation could also be expected from the derivation of the Cassie model based on an infinitesimal change of the interfacial areas, cf. Section 2. While the wetting properties of homogeneously structured surfaces (e.g. type I) can be discussed in terms of surface average properties, this approach fails for inhomogeneously structured surfaces (e.g. type II and III). In these cases, a local energy balance based on an infinitesimal change of the interfacial areas has to be applied to describe the contact angle adequately. That is, the average interfacial free energy does not describe the contact angle, if it is different from the local interfacial free energy in vicinity of the contact line.

4.3 Dynamic Wetting: Spreading of a Drop

In all scenarios considered in the present work, the system is initially in an unstable state in two regards: Firstly, the initial contact angle of 90° is larger than the intrinsic contact angle and, secondly, the grooves are not filled with fluid particles. As a consequence, the drop starts to spread

and the contact angle decreases. Since the impregnation wetting state is the energetically favorable state, the grooves start to fill.

The impregnation of the grooves underneath the drop is very fast. In all scenarios of the present study, it is accomplished in less than $5 \cdot 10^5$ time steps. On the walls of type I and type III, the grooves aside the drop fill by capillary condensation from the gas phase which occurs at a much slower rate. The grooves right next to the drop fill faster than the grooves further away. The amount of fluid condensing into the grooves is supplied by the liquid phase of the drop, i.e. the drop evaporates until the grooves are filled.

4.3.1 Scenarios on Walls I–2, II–2, II–6, and III–2

In the following, the spreading process is examined in detail for some of the simulation scenarios of the present study. The spreading of the drops of the scenarios I–2.32 and III–2.32 is shown in Figure 7. There, the contact line resides on the structured part of the walls with a groove width of $2\ \sigma$. With the start of the simulation, the drops start spreading as can be seen by the evolution of the contact line radius R_{sl} over time. The contact line advances more than $4\ \sigma$, i.e. over at least one groove pattern which consists of a groove and the adjacent rim. At the same time, the contact angle steadily decreases until a stable value is attained. After the decay, the value of the contact angle still fluctuates and the maximum and the minimum value of the instantaneous contact angle may differ by up to 6°. The speed of the spreading process is characterized by a decay time constant τ_1. That constant is determined by fitting the correlation

$$\theta(t) = \theta^{(1)} + (90° - \theta^{(1)}) \exp(-\frac{t}{\tau_1}) \tag{18}$$

to the simulation data for the contact angle, where the parameters are τ_1 and $\theta^{(1)}$. The fit results are given in Table 3. Good agreement between the correlation and the the simulation results is obtained, cf. Figure 7. In case of the scenario I–2.32 the value of the decay time constant is $1.7\ \tilde{t}$ and in case of the scenario III–2.32 it is $1.5\ \tilde{t}$. That is, the process of equilibration takes a time of

about 4.0 $\tilde{t}$ (or 4 million time steps) after which the drop attains a stable contact angle.

In the scenarios II–2.32 and II–6.32, a spreading process that is similar to the one before is observed, cf. Figure 8. The decay time constants are $\tau_1 = 1.1\ \tilde{t}$ for the scenario II–2.32 and $\tau_1 = 0.7\ \tilde{t}$ for the scenario II–6.32. The spreading is faster in the scenarios II–2.32 and II–6.32 than in the scenarios I–2.32 and III–2.32 which can be seen from the decay time constants. The faster spreading is attributed to the absence of grooves in the contact line region which pose hurdles to the spreading.

4.3.2 Scenarios on Walls I–6 and III–6

When the contact line advances over the grooves of 6 σ width, i.e. on the walls I–6 and III–6, the spreading process is different from that observed on the other walls. Figures 9 and 10 show the evolution of the contact line radius R_{sl} and the contact angle θ over time for different scenarios. While the results depend strongly on the drop size (cf. Figure 9 for smaller and Figure 10 for larger drops) there are no qualitative differences between the walls of type I and III, as expected. The time after which a stable contact angle is obtained is up to 25.0 $\tilde{t}$, which significantly exceeds the times observed for the scenarios on the other walls.

The comparison of Figure 9 with Figure 10 reveals different types of the courses of the time evolution of the contact angle and of the contact line radius. The different time evolutions depend on the drop size. In case of the small drops (scenarios I–6.38 and III–6.35, Figure 9) the instantaneous contact angle exhibits a rapid initial decay to a value of about 60° which is on the order of the intrinsic contact angle θ_0. After this initial decay, a slow and nearly linear decrease of the contact angle is observed between $t = 3.0\ \tilde{t}$ and $t = 22.0\ \tilde{t}$. Finally, the contact angle reaches a stable average value of 45° in case of scenario I–6.38 and $\theta = 43°$ in case of scenario III–6.35. In both scenarios, the evolution of the contact line radius over time indicates a rapid initial advance of the contact line, after which the final position is reached in scenario I–6.38 or which is followed by a slow receding motion in scenario III–6.35, cf. Figure 9 (top).

Figure 11 shows the configurations and the density profiles for the scenario I–6.38 at the times

$t = 2.5$, 13.0, and 31.0 $\tilde{t}$. In an early stage of the simulation, the drop does not fully cover the rim on which it is resting. The drop spreads, but there is not enough liquid that it could cover the entire rim. Instead, the drop forms liquid protrusions which may also cover the adjacent groove, which are filled by capillary condensation as discussed below in more detail. The formation of the protrusions leads to a continuous decay of the contact angle until a stable value of $\theta = 45°$ is reached. It can be seen in Figure 11 (middle) that the drop forms more than one protrusion. This was observed in most simulations of this type. While there are small protrusions which continuously form and vanish, the larger ones tend to survive and broaden. Over simulation time, protrusions coalesce so that in the scenario I–6.38 only a single protrusion remains, cf. Figure 11 (right).

Qualitatively, the spreading behavior described above for the scenarios I–6.38 and III–6.35 is also observed in the scenarios I–6.25 and I–6.36. The spreading process observed for the other scenarios with grooves of the width 6 σ, in which larger drops were studied, is different. There, a stick–slip spreading behavior with three phases is observed, cf. Figures 10 and 12 for the scenarios I–6.39 and III–6.41.

In scenario I–6.39, there is a rapid initial decrease of the contact angle up to $t = 3.0\ \tilde{t}$, cf. Figure 10, bottom. Then a small plateau is reached, on which the contact angle of about 68° changes little. A second phase of the spreading starts at about $t = 6.0\ \tilde{t}$ during which the contact angle decreases to its final value of 44°. The decrease of the contact angle goes along with an increase of the contact line radius R_{sl}, cf, Figures 10, top. After an initial increase of the contact line radius, it remains constant between $t = 3.0\ \tilde{t}$ and $6.0\ \tilde{t}$ and then increases until a radius of about 45 σ is reached.

The evolution of the contact angle and of the contact line radius which is observed in scenario III–6.41 is similar to scenario I–6.39. However, the initial spreading phase is faster and the plateau is reached already at $t = 0.5\ \tilde{t}$. The width of the plateau is again about $\Delta t = 3.0\ \tilde{t}$ and the final state is reached somewhat earlier than in the previous scenario. In the final state, the contact angles are similar in both scenarios, while the contact line radius is larger for scenario III–6.41, as there is more liquid available. The advance of the contact line radius in the second phase is 9 σ for the

larger drop (scenario III–6.41)and only about 6 σ for the smaller drop (scenario I–6.39).

As in all scenarios in which stick–slip like spreading behavior is observed, the contact line never shows a receding motion. Receding motion is solely observed in scenarios, in which the contact angle evolution exhibits a long linear decay.

In case of a stick–slip like spreading process which is solely observed in the scenarios on the walls I–6 and III–6, the course of the contact angle is described by the correlation

$$\theta(t) = \begin{cases} \theta^{(1)} + (90° - \theta^{(1)}) \exp(-\frac{t}{\tau_1}), & t \leq t_1 \\ \theta^{(2)} + (\theta^{(1)} - \theta^{(2)}) \exp(-\frac{t-t_1}{\tau_2}), & t > t_1 \end{cases} \tag{19}$$

which is similar to Eq. (18), but reflects the three observed phases of the spreading by two decay functions which are defined for different time periods. The parameters τ_1, τ_2, $\theta^{(1)}$, and $\theta^{(2)}$ are obtained from fitting the correlation to the simulation data. The parameter t_1 is chosen as the time at which the third spreading phase starts. For the two scenarios, the decay times of the first spreading phase ($\tau_1 \leq 1.2\ \tilde{t}$) are significantly smaller than the decay times of the second spreading phase which are between $\tau_2 = 3.0$ and $3.8\ \tilde{t}$, cf. Table 3.

Figure 12 shows the configurations and the density profiles for the scenario I–6.39 at the times $t = 2.5, 7.0, 28.0\ \tilde{t}$. The drop initially spreads on top of a rim until the contact line reaches the outer edge of the rim. The groove next to this rim is initially empty which corresponds to a Wenzel–like state, cf. Figure 12 (left). The contact line is pinned at the edge which corresponds to the plateaus in the time evolution of the contact line and the contact angle shown in Figure 10. If the contact line would spread over the empty groove, a large free energy would be required to form the new interfacial area. Thus, such spreading is not observed and the contact line is pinned, instead. While the contact line is pinned, capillary condensation fills the grooves and the Wenzel–like wetting state turns into the impregnation wetting state. The transition takes place via the formation of single nucleation sites in the grooves which further grow to droplets which then coalesce. Finally, the entire groove next to the drop is filled with fluid. After the groove is filled, the drop spontaneously forms a liquid protrusion bridging the the groove, see Figure 12 (middle). The liquid bridge broadens, i.e.

it spreads along the annulus and no contact line pinning occurs at this stage.[44] Thereby, the area of the plane liquid–vapor interface covering the grooves reduces which yields a reduction of the total interfacial free energy of the system. In some simulations, the broadening of the liquid protrusions leads to a full coverage of the groove next to the drop in the stable state. However, depending on the size of the drop, i.e. depending on the available liquid volume, the circumferential extent to which the drop covers a groove varies greatly. In the present study, the radial extent of the protrusions on the walls I–6 and III–6 was not found to exceed more than one groove and its adjacent rim. The circumferential location of the protrusions may continue to vary, even though the contact angle assumes a stable value. The asymmetric drop shapes observed during the spreading usually persist even in the stable state, cf. Figures 11 and 12. The stick–slip like spreading behavior is caused by the pinning of the contact line at the outer edge of a rim.

5 Conclusions

MD simulations have been carried out to study the static and the dynamic wetting properties of sessile drops on nanostructured walls in the impregnation wetting state. The walls have been structured by grooves arranged as concentric rings. The wall structure has been varied.

The dynamics of the spreading process is monitored and quantified by the decay time constant τ. Cases where the contact line moves on the plane wall are compared to cases where it moves on the structured parts of the wall. It is observed that the spreading is slower in the latter cases. For the scenarios on the walls I–6 and III–6, where the grooves have a width of 6 σ, the spreading process takes much longer than for the scenarios on the walls I–2 and III–2 where the groove width is only $B = 2\ \sigma$. In some scenarios on the walls I–6 and III–6, the spreading process also shows a stick–slip like behavior. The causes of this are revealed by monitoring the mechanisms of the drop spreading with high local and temporal resolution. The spreading is found be governed by the formation of liquid protrusions in combination with the capillary condensation of fluid into the grooves. The energetically favorable impregnation of the grooves with liquid leads to the formation of a liquid–vapor interface which covers the grooves. Subsequently, the drop spontaneously forms liquid protrusions which cover the grooves. This process leads to a favorable reduction of the interfacial free energy of the whole system. Finally, the liquid protrusions broaden along the circumferential direction of the grooves, a process which is not associated with a barrier in the free energy.[40] These observations corroborate the theory of de Gennes,[47] who claimed the formation and broadening of liquid protrusions as the actual mechanism of drop spreading on a structured wall. It is favored over the jump of the whole contact line, because the free energy barrier associated with the formation of liquid protrusions is lower.

In the scenarios on the walls I–6 and III–6, the occurrence of liquid protrusions usually leads to a shape and position of the drops which does not obey the symmetry imposed by the solid structure. This symmetry breaking behavior is retained even in the stationary state, in line with the results of a DFT study by Porcheron and Monson.[83]

In the stationary state, the contact angles of the drops on the homogeneously structured wall

I–2 ($B = 6\ \sigma$) are slightly larger than the intrinsic contact angle, which is in accord with previous molecular simulation and DFT studies.[65,66,68,69] The average contact angle of 44° on the homogeneously structured wall I–6 ($B = 6\ \sigma$) is significantly smaller than the intrinsic contact angle, in line with the result of a MC simulation study of a similar system.[65] The variation of the length of the structural pattern, i.e. the width B of a groove and the adjacent rim, from $B = 6\ \sigma$ to $B = 2\ \sigma$ leads to a crossover of the wetting properties of the structured walls. While the larger structures with $B = 6\ \sigma$ enhance the lyophilic nature of the wall, i.e. the contact angle is smaller due to the structure, the smaller structures ($B = 2\ \sigma$) exhibit the contrary effect. There, the lyophilic nature of the wall is reduced. This crossover is opposite to the Cassie model, which always predicts a decrease of the contact angle for drops in the impregnation state. Both for wall I–6 and for wall I–2, the Cassie model predicts a contact angle of $\theta_c = 38°$. Thus, the simulation results for the scenarios on wall I–2 contradict the Cassie model while the simulation results for the scenarios on wall I–6 are in qualitative agreement with that model.

In both cases, i.e. for the scenarios on the wall I–2 and I–6, the deviation of the simulation results from the prediction of the Cassie model can be interpreted in terms of the average surface-fluid free energy per unit area $\mathcal{F}$: The confinement of the liquid in the grooves leads to a deviation of the interfacial tensions from the values which would be observed on a macroscopic length scale. As a consequence, the value of $\mathcal{F}$ varies and so does the contact angle on the structure walls, cf. Eq. (8).

The present results obtained from MD simulations of sessile drops are consistent with the results obtained by sampling the interfacial free energy of the whole system using a MC technique. Thus, it can be concluded that the approach of describing the the contact angle on the basis of average free energies is appropriate if a homogeneous wall structure is present. In other words, there is no discrepancy between the free energy balance and the force balance if both are applied at the contact line, in contrast to the claim by Extrand[42] and Gao and McCarthy.[43]

In the present study, the observed contact angles in the stationary state on a particular wall vary in a narrow range which is a consequence of the low energy barrier caused by the formation

of liquid protrusions. A much stronger contact angle hysteresis has been observed in previous MD and DFT studies in which a liquid drop was replaced by a two–dimensional liquid cylinder.[45,84] The cylindrical shape of the liquid is stabilized by the application of periodic boundary conditions in the axial direction of the cylinder. Due to the comparatively short box length in the axial direction, the contact line is forced to jump as a whole over a surface patch which leads to very high energy barriers and to large contact angles just before a jump. The maximum contact angles observed in the cylindrical system[45,84] would not be observed in a three–dimensional systems, as the spreading mechanism via protrusions leads to smaller energy barriers.

The comparison of the contact angles of the drops on the walls of type II and III confirms that the Cassie model is inadequate for the prediction of contact angles if the walls are not homogeneously structured, in line with the experimental findings by Extrand[42] and Gao and McCarthy.[43] There, a local free energy balance in vicinity to the contact line must be applied to describe the contact angle. The results further demonstrate the need to precisely specify the surface structure by methods that are independent from the contact angle measurements. Otherwise, fitting the Cassie model to experimental contact angle data may yield a surface fraction ϕ without physical significance which cannot be used to predict the contact angles of different fluids or at varying thermodynamic conditions.

6 Acknowledgement

The authors gratefully acknowledge financial support by DFG within CRC 926 “Microscale Morphology of Component Surfaces”. Computational support is acknowledged by the Leibniz Supercomputing Center (LRZ) under the grant pr48te (“Sparlampe”) and by the Regional University Computing Center Kaiserslautern (RHRK) under the grant TUKL–MSWS. The present work was conducted under the auspices of the Boltzmann–Zuse Society for Computational Molecular Engineering (BZS).

References

(1) Young, T. An Essay on the Cohesion of Fluids. *Phil. Trans. R. Soc. Lond.* **1805**, *95*, 65–87.

(2) Frumkin, A. N. On the wetting phenomena and attachment of bubbles. *J. Phys. Chem. USSR* **1938**, *12*, 337–345.

(3) Fox, H.; Zisman, W. The spreading of liquids on low energy surfaces. I. Polytetrafluoroethylene. *J. Colloid Sci.* **1950**, *5*, 514 – 531.

(4) Fox, H. W.; Hare, E. F.; Zisman, W. A. Wetting Properties of Organic Liquids on High-Energy Surfaces. *J. Phys. Chem.* **1955**, *59*, 1097–1106.

(5) Israelachvili, J. N. van der Waals dispersion force contribution to works of adhesion and contact angles on the basis of macroscopic theory. *J. Chem. Soc., Faraday Trans. 2* **1973**, *69*, 1729–1738.

(6) Cahn, J. W. Critical point wetting. *J. Chem. Phys.* **1977**, *66*, 3667–3672.

(7) Hough, D. B.; White, L. R. The Calculation of Hamaker Constants from Liftshitz Theory with Applications to Wetting Phenomena. *Adv. Colloid Interface Sci.* **1980**, *14*, 3 – 41.

(8) Seemann, R.; Herminghaus, S.; Jacobs, K. Dewetting Patterns and Molecular Forces: A Reconciliation. *Phys. Rev. Lett.* **2001**, *86*, 5534–5537.

(9) Apte, P. A. Efficient computation of free energy of crystal phases due to external potentials by error–biased Bennett acceptance ratio method. *The Journal of Chemical Physics* **2010**, *132*, 084101.

(10) Israelachvili, J. N. *Intermolecular and Surface Forces*, 3rd ed.; Academic Press: San Diego, 2011.

(11) Nikolov, A.; Wasan, D. Wetting–dewetting films: The role of structural forces. *Adv. Colloid Interface Sci.* **2014**, *206*, 207 – 221, Manuel G. Velarde.

(12) Sikkenk, J. H.; Indekeu, J. O.; van Leeuwen, J. M. J.; Vossnack, E. O. Molecular-dynamics simulation of wetting and drying at solid-fluid interfaces. *Phys. Rev. Lett.* **1987**, *59*, 98–101.

(13) Sokolowski, S.; Fischer, J. Wetting transitions at the argon–solid–CO_2 interface: Molecular-dynamics studies. *Phys. Rev. A* **1990**, *41*, 6866–6870.

(14) Lundgren, M.; Allan, N. L.; Cosgrove, T.; George, N. Wetting of Water and Water/Ethanol Droplets on a Non-Polar Surface: A Molecular Dynamics Study. *Langmuir* **2002**, *18*, 10462–10466.

(15) Davidchack, R. L.; Laird, B. B. Direct calculation of the crystal–melt interfacial free energies for continuous potentials: Application to the Lennard–Jones system. *The Journal of Chemical Physics* **2003**, *118*, 7651–7657.

(16) Schneemilch, M.; Quirke, N. Effect of oxidation on the wettability of poly(dimethylsiloxane) surfaces. *J. Chem. Phys.* **2007**, *127*, 114701.

(17) Ingebrigtsen, T.; Toxvaerd, S. Contact Angles of Lennard-Jones Liquids and Droplets on Planar Surfaces. *J. Phys. Chem. C* **2007**, *111*, 8518–8523.

(18) Giovambattista, N.; Debenedetti, P. G.; Rossky, P. J. Effect of Surface Polarity on Water Contact Angle and Interfacial Hydration Structure. *J. Phys. Chem. B* **2007**, *111*, 9581–9587.

(19) Ohler, B.; Langel, W. Molecular Dynamics Simulations on the Interface between Titanium Dioxide and Water Droplets: A New Model for the Contact Angle. *J. Phys. Chem. C* **2009**, *113*, 10189–10197.

(20) Grzelak, E. M.; Shen, V. K.; Errington, J. R. Molecular Simulation Study of Anisotropic Wetting. *Langmuir* **2010**, *26*, 8274–8281.

(21) Becker, S.; Urbassek, H. M.; Horsch, M.; Hasse, H. Contact Angle of Sessile Drops in Lennard-Jones Systems. *Langmuir* **2014**, *30*, 13606–13614.

(22) Metya, A. K.; Khan, S.; Singh, J. K. Wetting Transition of the Ethanol–Water Droplet on Smooth and Textured Surfaces. *The Journal of Physical Chemistry C* **2014**, *118*, 4113–4121.

(23) Quéré, D. Wetting and Roughness. *Annu. Rev. Mater. Res.* **2008**, *38*, 71–99.

(24) Israelachvili, J. N.; Gee, M. L. Contact angles on chemically heterogeneous surfaces. *Langmuir* **1989**, *5*, 288–289.

(25) Cassie, A. B. D.; Baxter, S. Wettability of porous surfaces. *Trans. Faraday Soc.* **1944**, *40*, 546–551.

(26) Wenzel, R. N. Resistance of Solid Surfaces to Wetting by Water. *Ind. Eng. Chem.* **1936**, *28*, 988–994.

(27) Bartell, F. E.; Shepard, J. W. Surface Roughness as Related to Hysteresis of Contact Angles. II. The Systems Paraffin+Molar Calcium-Chloride Solution + Air and Paraffin+Glycerol+Air. *J. Phys. Chem.* **1953**, *57*, 455–458.

(28) Oliver, J.; Huh, C.; Mason, S. Resistance to spreading of liquids by sharp edges. *J. Colloid Interface Sci.* **1977**, *59*, 568 – 581.

(29) Oliver, J.; Huh, C.; Mason, S. An experimental study of some effects of solid surface roughness on wetting. *Colloids Surf.* **1980**, *1*, 79 – 104.

(30) Schwartz, L. W.; Garoff, S. Contact angle hysteresis on heterogeneous surfaces. *Langmuir* **1985**, *1*, 219–230.

(31) Shibuichi, S.; Onda, T.; Satoh, N.; Tsujii, K. Super Water-Repellent Surfaces Resulting from Fractal Structure. *J. Phys. Chem.* **1996**, *100*, 19512–19517.

(32) Bico, J.; Tordeux, C.; Quéré, D. Rough wetting. *Europhys. Lett.* **2001**, *55*, 214.

(33) Yong, X.; Zhang, L. T. Nanoscale Wetting on Groove-Patterned Surfaces. *Langmuir* **2009**, *25*, 5045–5053.

(34) Papadopoulos, P.; Mammen, L.; Deng, X.; Vollmer, D.; Butt, H.-J. Pinning–induced Variations of the Contact Angle of Drops on Microstructured Surfaces. *Chem. Lett.* **2012**, *41*, 1343–1345.

(35) Courbin, L.; Denieul, E.; Dressaire, E.; Roper, M.; Ajdari, A.; Stone, H. A. Imbibition by polygonal spreading on microdecorated surfaces. *Nat Mater* **2007**, *6*, 661–664.

(36) Kim, S. J.; Kim, J.; Moon, M.-W.; Lee, K.-R.; Kim, H.-Y. Experimental study of drop spreading on textured superhydrophilic surfaces. *Physics of Fluids* **2013**, *25*, 092105.

(37) Dettre, R. H.; Jr., R. E. J. Contact Angle Hysteresis. IV. Contact Angle Measurements on Heterogeneous Surfaces. *J. Phys. Chem.* **1965**, *69*, 1507–1515.

(38) He, B.; Lee, J.; Patankar, N. A. Contact angle hysteresis on rough hydrophobic surfaces. *Colloids Surf., A* **2004**, *248*, 101 – 104.

(39) Forsberg, P. S. H.; Priest, C.; Brinkmann, M.; Sedev, R.; Ralston, J. Contact Line Pinning on Microstructured Surfaces for Liquids in the Wenzel State. *Langmuir* **2010**, *26*, 860–865.

(40) Johnson, R. E.; Dettre, R. H. Contact Angle Hysteresis. III. Study of an Idealized Heterogeneous Surface. *J. Phys. Chem.* **1964**, *68*, 1744–1750.

(41) Marmur, A.; Bittoun, E. When Wenzel and Cassie Are Right: Reconciling Local and Global Considerations. *Langmuir* **2009**, *25*, 1277–1281.

(42) Extrand, C. W. Contact Angles and Hysteresis on Surfaces with Chemically Heterogeneous Islands. *Langmuir* **2003**, *19*, 3793–3796.

(43) Gao, L.; McCarthy, T. J. How Wenzel and Cassie Were Wrong. *Langmuir* **2007**, *23*, 3762–3765.

(44) Johnson, R. E.; Dettre, R. H. In *Contact Angle, Wettability, and Adhesion*; Fowkes, F. M., Ed.; American Chemical Society: Washington, D.C., 1964; Chapter 8, pp 112–135.

(45) Berim, G. O.; Ruckenstein, E. Nanodrop on a nanorough solid surface: Density functional theory considerations. *J. Chem. Phys.* **2008**, *129*, 014708.

(46) Shahraz, A.; Borhan, A.; Fichthorn, K. A. Wetting on Physically Patterned Solid Surfaces: The Relevance of Molecular Dynamics Simulations to Macroscopic Systems. *Langmuir* **2013**, *29*, 11632–11639.

(47) de Gennes, P. G. Wetting: Statics and dynamics. *Rev. Mod. Phys.* **1985**, *57*, 827–863.

(48) Grzelak, E. M.; Errington, J. R. Computation of interfacial properties via grand canonical transition matrix Monte Carlo simulation. *The Journal of Chemical Physics* **2008**, *128*, 014710.

(49) Laird, B. B.; Davidchack, R. L. Calculation of the interfacial free energy of a fluid at a static wall by Gibbs–Cahn integration. *The Journal of Chemical Physics* **2010**, *132*, 204101.

(50) Rane, K. S.; Kumar, V.; Errington, J. R. Monte Carlo simulation methods for computing the wetting and drying properties of model systems. *J. Chem. Phys.* **2011**, *135*, 234102.

(51) Evans, R. Fluids adsorbed in narrow pores: phase equilibria and structure. *J. Phys.: Cond. Mat.* **1990**, *2*, 8989.

(52) Chen, L.-J. Area dependence of the surface tension of a Lennard–Jones fluid from molecular dynamics simulations. *J. Chem. Phys.* **1995**, *103*, 10214–10216.

(53) Brovchenko, I.; Oleinikova, A. Molecular organization of gases and liquids at solid surfaces. *Handbook of Theoretical and Computational Nanotechnology* **2005**, *9*, 109–206.

(54) Liu, Y.; Panagiotopoulos, A. Z.; Debenedetti, P. G. Finite–size scaling study of the vapor–liquid critical properties of confined fluids: Crossover from three dimensions to two dimensions. *J. Chem. Phys.* **2010**, *132*, 144107.

(55) Singh, S. K.; Singh, J. K. Effect of pore morphology on vapor–liquid phase transition and crossover behavior of critical properties from 3D to 2D. *Fluid Phase Equilib.* **2011**, *300*, 182 – 187.

(56) Khan, S.; Singh, J. K. Wetting transition of nanodroplets of water on textured surfaces: a molecular dynamics study. *Molecular Simulation* **2014**, *40*, 458–468.

(57) Fu, D. Investigation of excess adsorption, solvation force, and plate–fluid interfacial tension for Lennard–Jones fluid confined in slit pores. *J. Chem. Phys.* **2006**, *124*, 164701.

(58) Hamada, Y.; Koga, K.; Tanaka, H. Phase equilibria and interfacial tension of fluids confined in narrow pores. *J. Chem. Phys.* **2007**, *127*, 084908.

(59) Singh, J. K.; Kwak, S. K. Surface tension and vapor–liquid phase coexistence of confined square–well fluid. *J. Chem. Phys.* **2007**, *126*, 024702.

(60) Singh, S. K.; Sinha, A.; Deo, G.; Singh, J. K. Vapor–Liquid Phase Coexistence, Critical Properties, and Surface Tension of Confined Alkanes. *J. Phys. Chem. C* **2009**, *113*, 7170–7180.

(61) Werth, S.; Lishchuk, S. V.; Horsch, M.; Hasse, H. The influence of the liquid slab thickness on the planar vapor–liquid interfacial tension. *Physica A* **2013**, *392*, 2359 – 2367.

(62) Dutta, R. C.; Khan, S.; Singh, J. K. Wetting transition of water on graphite and boron–nitride surfaces: A molecular dynamics study. *Fluid Phase Equilib.* **2011**, *302*, 310 – 315, 12th International Conference on Properties and Phase Equilibria for Product and Process Design.

(63) Santiso, E. E.; Herdes, C.; Müller, E. A. On the Calculation of Solid-Fluid Contact Angles from Molecular Dynamics. *Entropy* **2013**, *15*, 3734–3745.

(64) Grzelak, E. M.; Errington, J. R. Nanoscale Limit to the Applicability of Wenzel's Equation. *Langmuir* **2010**, *26*, 13297–13304.

(65) Kumar, V.; Errington, J. R. Impact of Small-Scale Geometric Roughness on Wetting Behavior. *Langmuir* **2013**, *29*, 11815–11820.

(66) Tang, J. Z.; Harris, J. G. Fluid wetting on molecularly rough surfaces. *J. Chem. Phys.* **1995**, *103*, 8201–8208.

(67) Malanoski, A. P.; Johnson, B. J.; Erickson, J. S. Contact angles on surfaces using mean field theory: nanodroplets vs. nanoroughness. *Nanoscale* **2014**, *6*, 5260–5269.

(68) Malijevský, A. Does surface roughness amplify wetting? *J. Chem. Phys.* **2014**, *141*, 184703.

(69) Svoboda, M.; Malijevský, A.; Lisal, M. Wetting properties of molecularly rough surfaces. *J. Chem. Phys.* **2015**, *143*, 104701.

(70) Leroy, F.; Müller-Plathe, F. Rationalization of the Behavior of Solid–Liquid Surface Free Energy of Water in Cassie and Wenzel Wetting States on Rugged Solid Surfaces at the Nanometer Scale. *Langmuir* **2011**, *27*, 637–645.

(71) Li, Z.; Liao, K.; Liao, F.; Xiao, Q.; Jiang, F.; Zhang, X.; Liu, B.; Sun, C.; Chen, G. Wetting and Spreading Behaviors of Nanodroplets: The Interplay Among Substrate Hydrophobicity, Roughness, and Surfactants. *The Journal of Physical Chemistry C* **2016**, *120*, 15209–15215.

(72) Wang, F.; Wu, H. Molecular origin of contact line stick-slip motion during droplet evaporation. *Scientific Reports* **2015**, *5*, 17521.

(73) Allen, M.; Tildesley, D. *Computer Simulation of Liquids*; Clarendon: Oxford, 2009.

(74) Vrabec, J.; Kedia, G. K.; Fuchs, G.; Hasse, H. Comprehensive study of the vapour–liquid coexistence of the truncated and shifted Lennard–Jones fluid including planar and spherical interface properties. *Mol. Phys.* **2006**, *104*, 1509–1527.

(75) van Meel, J. A.; Page, A. J.; Sear, R. P.; Frenkel, D. Two–step vapor–crystal nucleation close below triple point. *J. Chem. Phys.* **2008**, *129*, 204505.

(76) Niethammer, C.; Becker, S.; Bernreuther, M.; Buchholz, M.; Eckhardt, W.; Heinecke, A.; Werth, S.; Bungartz, H.-J.; Glass, C. W.; Hasse, H. et al. ls1 mardyn: The Massively Parallel Molecular Dynamics Code for Large Systems. *J. Chem. Theory Comput.* **2014**, *10*, 4455–4464.

(77) Andersen, H. C. Molecular dynamics simulations at constant pressure and/or temperature. *The Journal of Chemical Physics* **1980**, *72*, 2384–2393.

(78) Oleinikova, A.; Brovchenko, I.; Geiger, A. Behavior of a wetting phase near a solid boundary: vapor near a weakly attractive surface. *Eur. Phys. J. B* **2006**, *52*, 507–519.

(79) Krone, M.; Stone, J.; Ertl, T.; Schulten, K. Fast Visualization of Gaussian Density Surfaces for Molecular Dynamics and Particle System Trajectories. EuroVis – Short Papers. 2012.

(80) Rowlinson, J.; Widom, B. *Molecular Theory of Capillarity*; Dover Publications, 2002.

(81) Nijmeijer, M. J. P.; Bruin, C.; Bakker, A. F.; van Leeuwen, J. M. J. Wetting and drying of an inert wall by a fluid in a molecular-dynamics simulation. *Phys. Rev. A* **1990**, *42*, 6052–6059.

(82) Leroy, F.; Müller-Plathe, F. Solid-liquid surface free energy of Lennard-Jones liquid on smooth and rough surfaces computed by molecular dynamics using the phantom-wall method. *J. Chem. Phys.* **2010**, *133*, 044110.

(83) Porcheron, F.; Monson, P. A.; Schoen, M. Wetting of rings on a nanopatterned surface: A lattice model study. *Phys. Rev. E* **2006**, *73*, 041603.

(84) Shahraz, A.; Borhan, A.; Fichthorn, K. A. A Theory for the Morphological Dependence of Wetting on a Physically Patterned Solid Surface. *Langmuir* **2012**, *28*, 14227–14237.

Figures

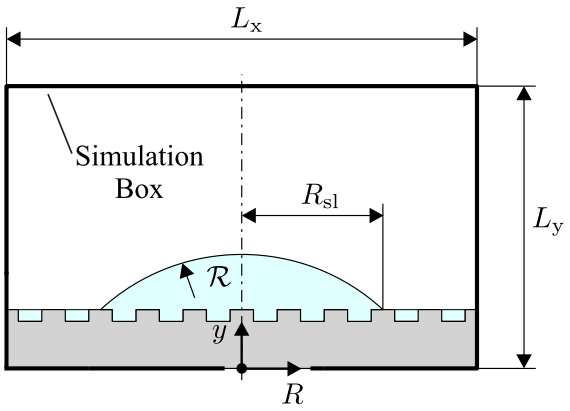

Figure 1: Sketch of the simulation scenarios.

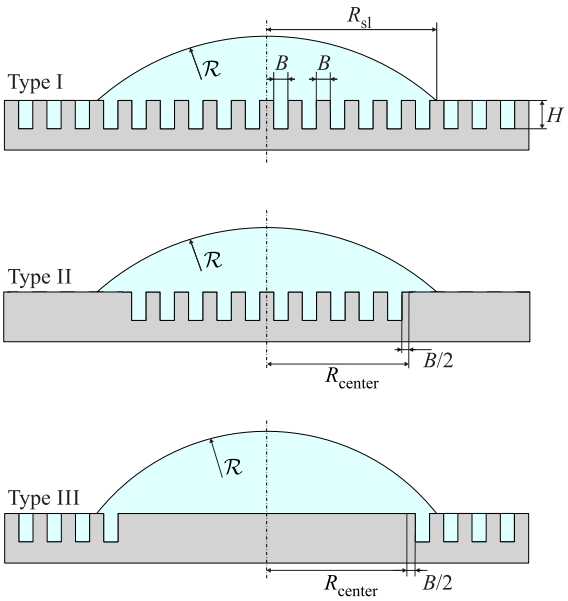

Figure 2: Schematic sketch of the structured walls used in the present work. The dash–dot line represents the symmetry axis of the concentric rings. There are three types of walls, designated by I, II, and III, which differ in the arrangement of the grooves. Their designation is given in Table 1.

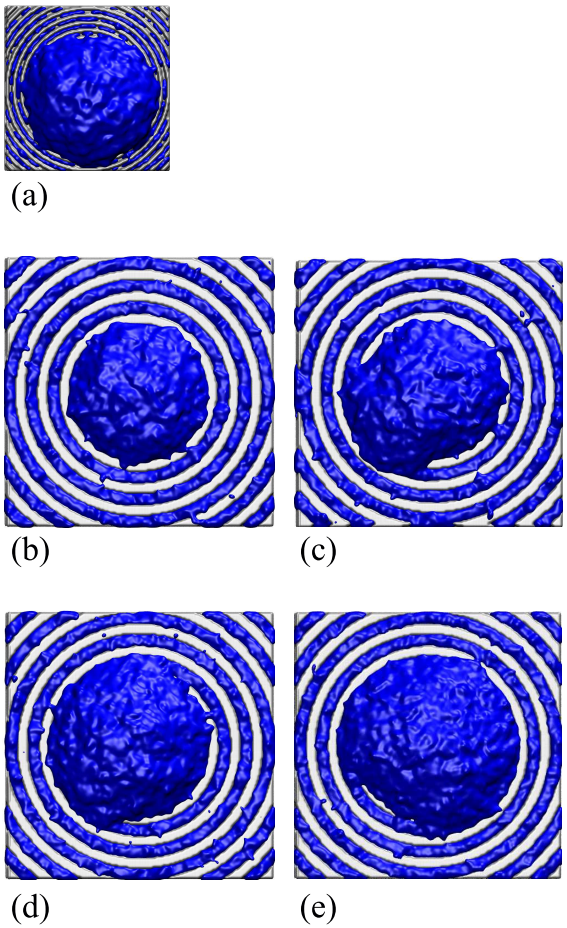

Figure 3: Snapshots of sessile drops from five simulation runs. Each snapshot shows the configuration at the end of the simulation run. The particular scenarios are: I–2.32 at $t = 12.0\ \tilde{t}$ (a), I–6.36 at $t = 30.0\ \tilde{t}$ (b), I–6.38 at $t = 31.0\ \tilde{t}$ (c), I–6.39 at $t = 28.0\ \tilde{t}$ (d), and I–6.40 at $t = 25.0\ \tilde{t}$ (e). The lateral dimension of the wall I–2 (a) is $L_x = L_z = 89.8\ \sigma$ and that of wall I–6 (b-e) is $L_x = L_z = 145.5\ \sigma$.

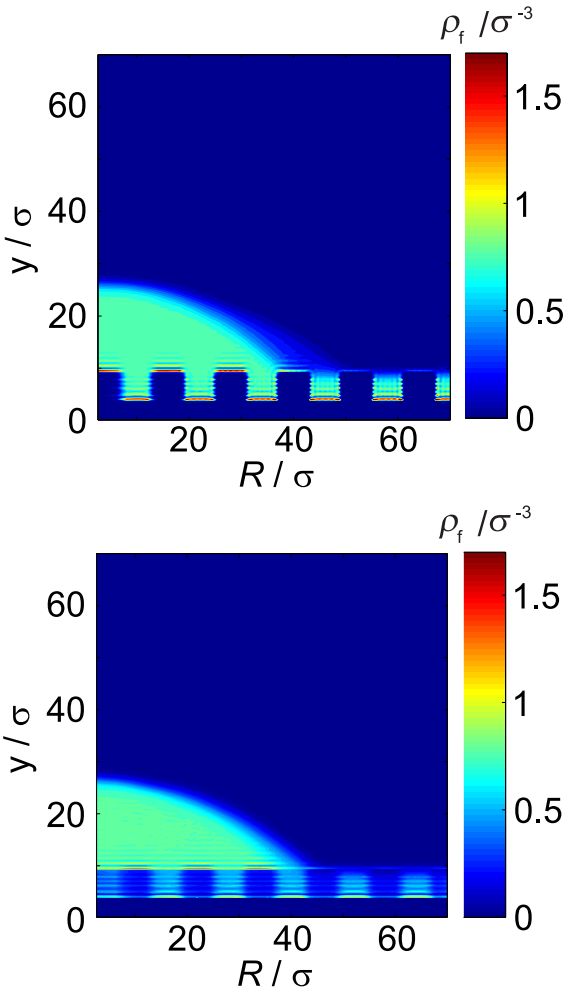

Figure 4: Density profiles of the fluid in the wall–fixed coordinate system (top) and in the drop–fixed coordinate system (bottom). Both density profiles are obtained from scenario I–6.38 after $t = 31.0\,\tilde{t}$, cf. Figure 3 (right).

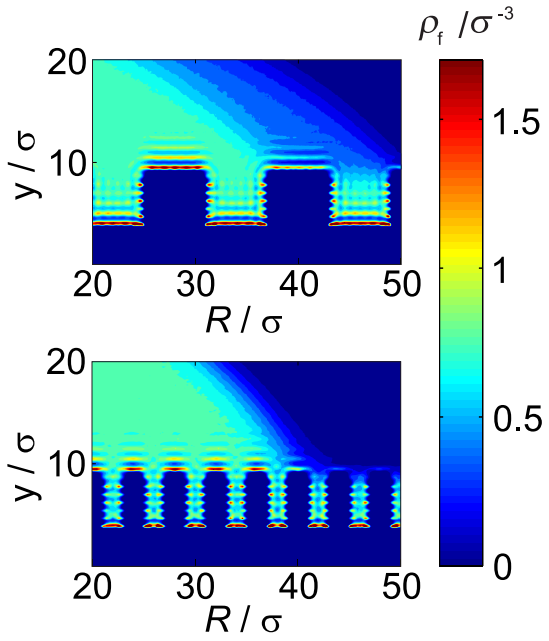

Figure 5: Density profiles of the fluid in the wall–fixed coordinate system. Top: Grooves of width $B = 6\ \sigma$ (wall I-6). Bottom: Grooves of width $B = 2\ \sigma$ (wall I-2). In both cases, the fluid fills the grooves and a layered ordering of the fluid can be observed.

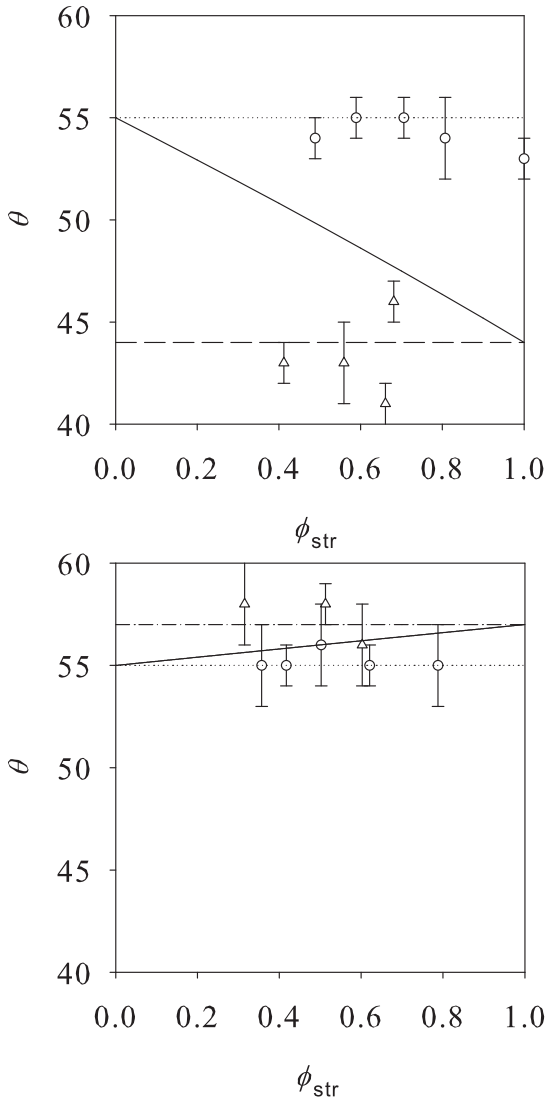

Figure 6: Contact angle θ versus the structured surface fraction ϕ_{str}. Top: The two types of composite walls with a groove width of $B = 6\,\sigma$. Simulation: (∘) wall II–6, (△) wall III–6. Bottom: The two types of composite walls with a groove width of $B = 2\,\sigma$. Simulation: (∘) wall II–2, (△) wall III–2. Lines: (·····) intrinsic contact angle, (− − −) average contact angle on wall I–6, (— · —) average contact angle on wall I–2, (———) prediction by Eq. (14), cf. Section 4.2.5.

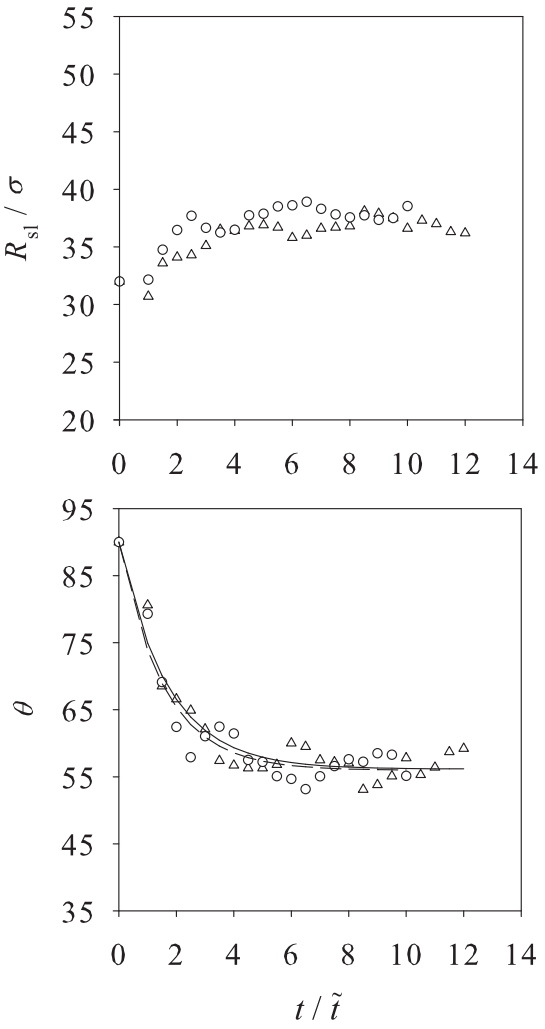

Figure 7: Spreading process in the scenarios I–2.32 (△) and III–2.32(∘). Top: Contact line radius R_{sl} versus time, bottom: Contact angle θ versus time.

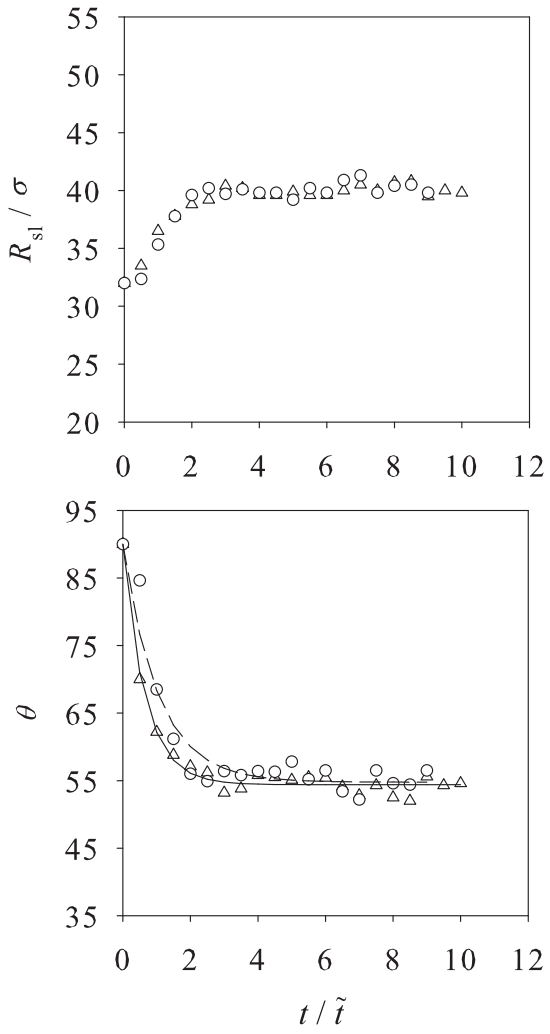

Figure 8: Spreading process in the scenarios II–2.32 (∘) and II–6.32 (△). Top: Contact line radius R_{sl} versus time, bottom: Contact angle θ versus time.

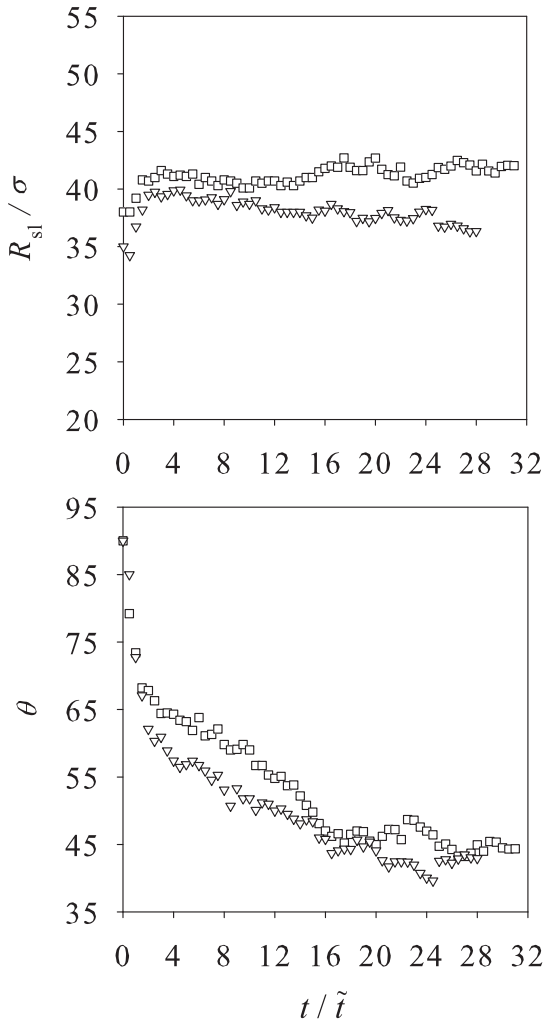

Figure 9: Spreading process in the scenarios I–6.38 (□) and III–6.35 (▽). Top: Contact line radius R_{sl} versus time, bottom: Contact angle θ versus time.

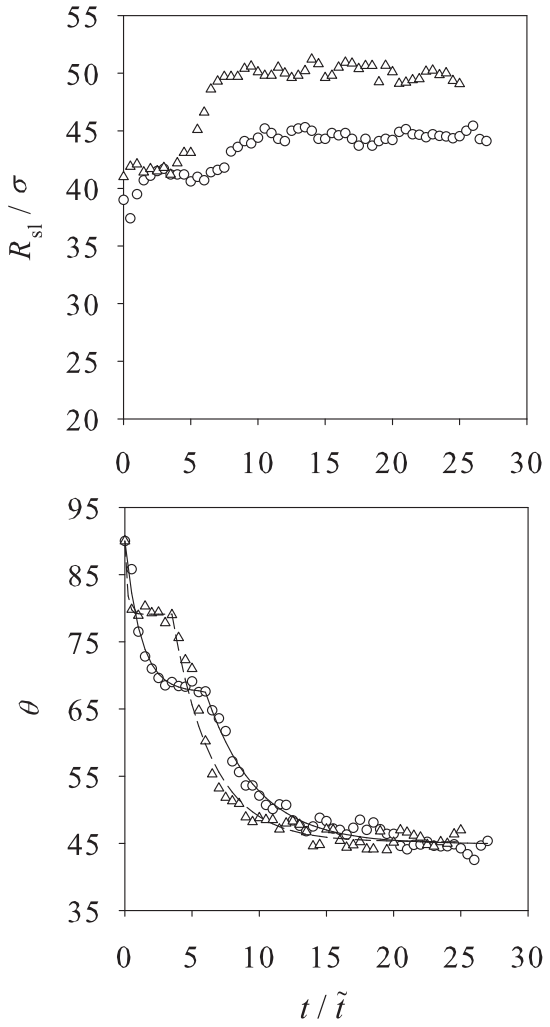

Figure 10: Spreading $t/\tilde{t}$ process in the scenarios I–6.39 (∘) and III–6.41 (△). Top: Contact line radius R_{sl} versus time, bottom: Contact angle θ versus time.

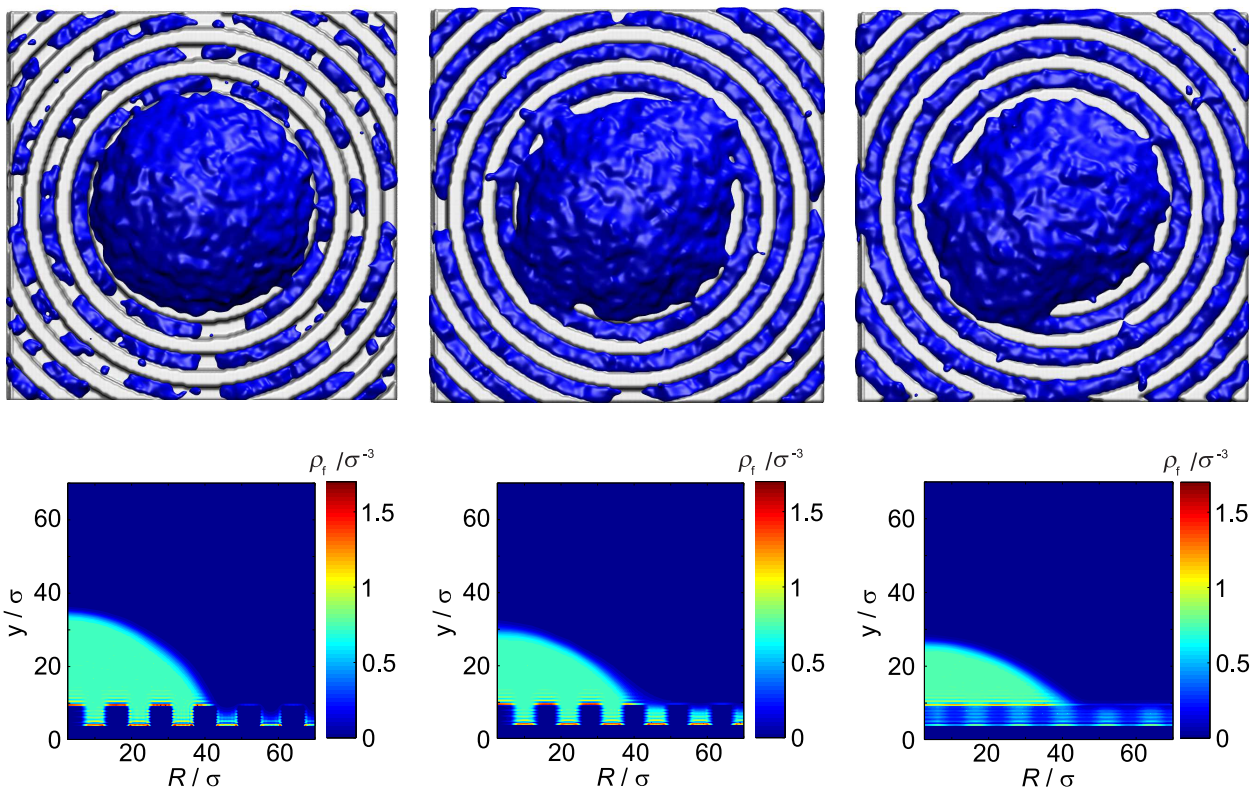

Figure 11: Spreading of the drop of Scenario I–6.38. The top row shows snapshots taken during the simulation where the representation of the molecules by single particles is replaced by surfaces representing iso–values of the density. From left to right, the time is advancing and the snapshots are taken after $t = 2.5$, 13.0, and 31.0 $\tilde{t}$. At the bottom row, the density profiles of the fluid are shown.

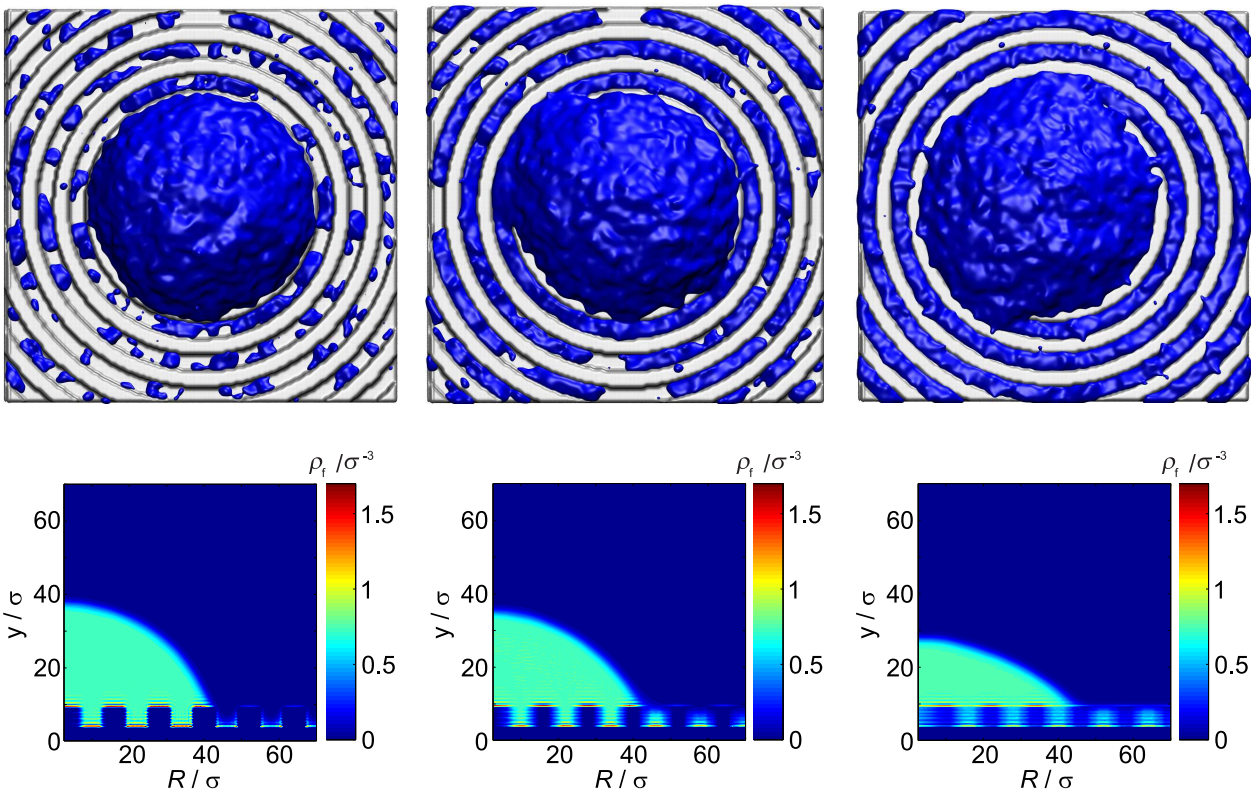

Figure 12: Spreading of the drop in scenario I–6.39. The top row shows snapshots taken during the simulation where the representation of the molecules by single particles is replaced by surfaces representing iso–values of the density. From left to right, the time is advancing and the snapshots are taken after $t = 2.5, 7.0$, and $28.0\,\tilde{t}$. In the bottom row, the density profiles of the fluid component are shown.

Tables

Table 1: The wall morphologies used in the present study are characterized by the width of the grooves B, the innermost groove radius λ_1, and in case of the composite walls by the radii R_{center}.

Wall	B/σ	λ_1/σ	R_{center}/σ
I–6	6	7	-
I–2	2	1	-
II–6	6	7	28
II–2	2	1	24
III–6	6	31	28
III–2	2	25	24

Table 2: Initial radius $\mathcal{R}^{(0)}$ and simulation results of the scenarios in the stationary state: Contact angle θ, drop volume V, and radius of the solid–liquid interface R_{sl}.

Scenario	$\mathcal{R}^{(0)}/\sigma$	$\theta/°$	R_{sl}/σ	$V/1000\sigma^3$	Scenario	$\mathcal{R}^{(0)}/\sigma$	$\theta/°$	R_{sl}/σ	$V/1000\sigma^3$
I–6.25	25	45±2	26.1±0.4	12.4±0.1	I–2.25	25	55±1	23.1±0.2	11.0±0.2
I–6.36	36	43±1	37.6±0.7	34.5±0.8	I–2.27	27	59±2	27.4±1.1	19.4±0.6
I–6.38	38	45±2	41.7±0.5	49.9±0.4	I–2.28	28	58±1	29.2±0.3	24.1±0.2
I–6.39	39	44±1	44.6±0.4	60.0±0.5	I–2.29	29	58±2	31.3±0.4	29.2±0.2
I–6.40	40	42±1	47.8±0.5	69.7±0.5	I–2.32	32	56±2	37.0±0.6	46.8±0.2
II–6.24	24	53±1	27.9±0.4	18.4±0.1	II–2.24	24	55±2	27.0±0.5	17.7±0.2
II–6.26	26	54±2	31.2±0.5	25.5±2.4	II–2.26	26	55±1	30.5±0.3	25.1±0.3
II–6.28	28	55±1	33.3±0.4	32.9±0.3	II–2.28	28	56±2	33.9±0.5	35.1±0.3
II–6.30	30	55±1	36.5±0.4	42.9±0.3	II–2.30	30	55±1	37.2±0.3	45.3±0.3
II–6.32	32	54±1	40.1±0.5	56.0±0.2	II–2.32	32	55±2	40.2±0.6	58.2±0.3
III–6.35	35	43±1	36.5±0.3	31.3±0.3	III–2.27	27	58±2	29.0±0.4	23.5±0.1
III–6.37	37	43±2	42.2±0.6	48.3±0.4	III–2.30	30	58±3	34.4±0.8	39.2±0.3
III–6.39	39	41±1	48.1±0.4	67.5±0.6	III–2.32	32	56±2	38.1±0.6	50.6±0.4
III–6.41	41	46±1	49.6±0.4	85.8±0.3					

Table 3: Parameters τ_1, $\theta^{(1)}$, t_1, τ_2, and $\theta^{(2)}$ according to Eqs. (18) and (19) characterizing the contact angle dynamics.

Scenario	$\theta^{(1)}/°$	$\tau_1/\tilde{t}$	$t_1/\tilde{t}$	$\theta^{(2)}/°$	$\tau_2/\tilde{t}$
I–2.32	56	1.7			
III–2.32	58	1.5			
II–2.32	55	1.1			
II–6.32	54	0.7			
I–6.39	68	1.2	6.0	45	3.8
III–6.41	80	0.2	3.5	45	3.0

Table A.1: Specification of the simulation scenarios of the present work by the total number of particles N, the number of fluid particles N_f, the simulation box length in x, z–direction $L_x = L_z$, and the simulation box length in y-direction L_y.

Scenario	N	N_f	L_x/σ	L_y/σ
I–6.25	74464	27900	80.5	49.8
I–6.36	248794	99254	145.5	82.8
I–6.38	260803	111263	145.5	82.8
I–6.39	267382	117842	145.5	82.8
I–6.40	273403	123863	145.5	81.8
I–2.25	87116	29870	89.8	54.8
I–2.27	93096	35850	89.8	54.8
I–2.28	96604	39358	89.8	54.8
I–2.29	100183	42937	89.8	54.8
I–2.32	112647	55401	89.8	54.8
II–6.24	83436	25594	80.5	50.8
II–6.26	89000	31158	80.5	50.8
II–6.28	136404	42058	100.6	59.8
II–6.30	103160	45318	80.5	50.8
II–6.32	111473	53631	80.5	50.8
II–2.24	125885	29783	100.6	59.8
II–2.26	131462	35360	100.6	59.8
II–2.28	138160	42058	100.6	59.8
II–2.30	145205	49103	100.6	59.8
II–2.32	154330	58228	100.6	59.8
III–6.35	249663	93069	145.5	82.8
III–6.37	261659	105065	145.5	82.8
III–6.39	274436	274290	145.5	82.8
III–6.41	288402	131808	145.5	82.8
III–2.27	98394	35850	89.8	54.8
III–2.30	109505	46961	89.8	54.8
III–2.32	117945	55401	89.8	54.8

Graphical TOC Entry